J. Fluid Mech. (2010), *vol.* 657, *pp.* 126–170.
doi:10.1017/S0022112010001412

Transverse instability of surface solitary waves. Part 2. Numerical linear stability analysis

TAKESHI KATAOKA†

Department of Mechanical Engineering, Graduate School of Engineering, Kobe University,
Rokkodai, Nada, Kobe 657-8501, Japan

(Received 10 November 2009; revised 14 March 2010; accepted 15 March 2010;

In a previous work, Kataoka & Tsutahara (*J. Fluid Mech.*, vol. 512, 2004*a*, p. 211) proved the existence of longitudinally stable but transversely unstable surface solitary waves by asymptotic analysis for disturbances of small transverse wavenumber. In the present paper, the same transverse instability is examined numerically for the whole range of solitary-wave amplitudes and transverse wavenumbers of disturbances. Numerical results show that eigenvalues and eigenfunctions of growing disturbance modes agree well with those obtained by the asymptotic analysis if the transverse wavenumber of the disturbance is small. As the transverse wavenumber increases, however, the growth rate of the disturbance, which is an increasing function for small wavenumbers, reaches a maximum and finally falls to zero at some finite wavenumber. Thus, there is a high-wavenumber cutoff to the transverse instability. For higher amplitude, solitary waves become longitudinally unstable, and the dependence of the eigenvalues on the transverse wavenumber exhibits various complicated patterns. We found that such eigenvalues versus transverse wavenumber can be simply grouped into three basic classes.

1. Introduction

In a system under uniform gravitational acceleration, surface solitary waves propagate on a free surface of fluid of finite depth. Their surface profile is represented by a single hump of elevation with a straight crest, and their properties were first calculated numerically by Byatt-Smith & Longuet-Higgins (1976) and later by Tanaka (1986) and Longuet-Higgins & Tanaka (1997) on the basis of the Euler set of equations. The wave speed, energy, etc. were obtained as functions of the wave amplitude h, which is defined as the ratio of the maximum surface elevation to average depth of the fluid. Wave properties result in oscillations with rapidly decreasing period as h approaches the limiting value 0.83322 (Longuet-Higgins & Fox 1996). Here we are interested in the linear stability of surface solitary waves to three-dimensional disturbances (so-called transverse stability). Before mentioning the aims of the present study, let us briefly outline previous work on the stability of surface solitary waves.

Jeffrey & Kakutani (1970) and Benjamin (1972) made linear stability analyses of small-amplitude solitary waves. They investigated the stability to two-dimensional disturbances that have no dependence on the transverse direction (so-called longitudinal stability). The celebrated Korteweg–de Vries (KdV) equation was used

---

† Email address for correspondence: kataoka@mech.kobe-u.ac.jp

as a basic equation, and it was found that small-amplitude solitary waves are longitudinally stable. Study of transverse stability was initiated by Kadomtsev & Petviashvili (1970). They derived the Kadomtsev–Petviashvili (KP) equation, which is a three-dimensional extension of the KdV equation, and on the basis of this equation, made a linear stability analysis with respect to three-dimensional disturbances (see also Zakharov 1975; Kuznetsov, Spector & Fal'Kovich 1984; Alexander, Pego & Sachs 1997; Allen & Rowlands 1997; Kivshar & Pelinovsky 2000). It was revealed that small-amplitude solitary waves without surface-tension effects are stable not only longitudinally but also transversely.

The stability of finite-amplitude surface solitary waves was first examined by Tanaka (1986). He investigated numerically the linear stability to two-dimensional disturbances (longitudinal stability), and found that an exchange of longitudinal stability occurs at $h = 0.7807$. This wave amplitude corresponds to the first extremum in the energy of the solitary wave. Tanaka *et al.* (1987) also simulated the time development of an unstable solitary wave. The time evolution is largely dependent on the sign of a growing disturbance mode added to the solitary wave. In one case, it leads to wave breaking; in the other case, it undergoes a transition to a lower solitary wave having almost the same energy. Longuet-Higgins & Tanaka (1997) carried out a detailed linear stability analysis and showed numerically that a second exchange of stabilities occurs at the second extremum in the energy of the solitary wave. An analytical proof was finally given by Kataoka (2006*a*) that the exchange of stabilities occurs at every extremum in the wave energy, as in the case of surface periodic waves (Saffman 1985; Kataoka 2006*b*). In this way, the longitudinal stability of surface solitary waves has been elucidated so far.

On the other hand, it was only recently that the study of transverse stability of finite-amplitude surface solitary waves began. Bridges (2001) examined the transverse stability analytically in the case of long-wavelength transverse disturbances. His analysis is, however, based on the leading-order effects of small wavenumbers only, and could not find any transverse instability for $h < 0.7807$. The higher-order effects of the small transverse wavenumbers were appropriately taken into account later by Kataoka & Tsutahara (2004*a*) using a systematic asymptotic analysis for disturbances of small transverse wavenumber, and it was revealed that there exist longitudinally stable but transversely unstable surface solitary waves for $0.7133 < h < 0.7807$. Their analysis is based on the full Euler set of equations. The only assumption is that the transverse wavenumber of the disturbance should be small. It is thus desired to examine how this transverse instability changes as the transverse wavenumber of the disturbance becomes larger.

In the present study, therefore, we have carried out a numerical linear stability analysis of finite-amplitude surface solitary waves on the basis of the three-dimensional full Euler set of equations. We clarified the transverse stability not only for the longitudinally stable range $h < 0.7807$ but also for the whole range of solitary-wave amplitudes and transverse wavenumbers of the disturbances. To the best of our knowledge, this is the first study to examine the transverse stability of finite-amplitude surface solitary waves numerically (see McLean 1982*a*, *b* for the case of surface periodic waves). The numerical method is based on a boundary-element method which utilizes Green's function of the modified Helmholtz equation. Numerical results show that, if the transverse wavenumber of the disturbance is small, eigenvalues and eigenfunctions of growing disturbance modes agree well with those obtained by the asymptotic analysis for small transverse wavenumbers of disturbances. As the transverse wavenumber increases, however, there is a high-wavenumber cutoff to the transverse instability. This means that transversely unstable solitary waves are stable to a disturbance of wavenumber higher than some critical value. For the longitudinally unstable solitary waves ($h > 0.7807$), eigenvalues of growing disturbance modes depend on their transverse wavenumbers in various complicated ways. We arrange their patterns into three basic classes in terms of the signs of two parameters of the solitary wave, and further into six by distinguishing three marginal classes that occur in a limited range of wave amplitudes.

The outline of this paper is as follows. We formulate the basic equations in § 2, where the problem of stability is reduced to a linear eigenvalue problem. The numerical method is described in § 3. Numerical results on eigenvalues and eigenfunctions (or surface profiles of growing disturbance modes) are presented in §§ 4 and 5, respectively, and concluding remarks follow in § 6. The asymptotic solution obtained by Kataoka & Tsutahara (2004*a*) and Kataoka (2008) is valid for broad ranges but does not give good approximation in the special cases where the energy or the wave speed of the solitary wave is near its extremum. We present asymptotic solutions valid only for these cases in Appendices A and B.

2. Formulation

Consider irrotational motion of an incompressible ideal fluid of undisturbed depth D with a free surface under uniform gravitational acceleration g. The effects of surface tension are neglected. In what follows, all variables are non-dimensionalized using g and D. Let x, y and z be the Cartesian coordinates, with the z-axis pointing vertically upwards and their origin being placed on an undisturbed free surface. The fluid motion is governed by

$$\frac{\partial^2\phi}{\partial x^2}+\frac{\partial^2\phi}{\partial y^2}+\frac{\partial^2\phi}{\partial z^2}=0 \quad \text{for} \quad -1<z<\eta, \tag{2.1}$$

with boundary conditions

$$\frac{\partial\eta}{\partial t}+\frac{\partial\phi}{\partial x}\frac{\partial\eta}{\partial x}+\frac{\partial\phi}{\partial y}\frac{\partial\eta}{\partial y}=\frac{\partial\phi}{\partial z} \quad \text{at} \quad z=\eta, \tag{2.2}$$

$$\frac{\partial\phi}{\partial t}+\frac{1}{2}\left[\left(\frac{\partial\phi}{\partial x}\right)^2+\left(\frac{\partial\phi}{\partial y}\right)^2+\left(\frac{\partial\phi}{\partial z}\right)^2\right]+\eta=b(t) \quad \text{at} \quad z=\eta, \tag{2.3}$$

$$\frac{\partial\phi}{\partial z}=0 \quad \text{at} \quad z=-1, \tag{2.4}$$

where t is time, $\phi(x,\ y,\ z,\ t)$ is the velocity potential, $\eta(x,\ y,\ t)$ is the surface elevation and $b(t)$ is a function of t which is determined by evaluating (2.3) as $x\rightarrow\infty$.

We first consider a solution of (2.1)–(2.4) that is independent of t and y:

$$\phi=-vx+\Phi_s(x,z), \qquad \eta=\eta_s(x), \tag{2.5a, b}$$

where v is a positive real parameter, and $\partial\Phi_s/\partial x$, $\partial\Phi_s/\partial z$ and η_s decay as $x\rightarrow\pm\infty$. The solution (2.5) represents a steady propagation of a two-dimensional localized wave against a uniform stream of constant velocity $-v$ in the x direction. We call this solution a solitary wave solution. The existence of this solution has been numerically confirmed for $1<v<1.2942$ (Byatt-Smith & Longuet-Higgins 1976; Tanaka 1986; Longuet-Higgins & Tanaka 1997). In terms of the maximum surface elevation

$$h=\max(\eta_s), \tag{2.6}$$

the range of existence is $0 < h < 0.83322$. Depending on the situation, we use either v or h as an independent parameter to characterize the solitary wave. The solitary wave solution has the property that the surface elevation η_s (>0) possesses a single point of extremum which is called the crest. Moreover, the solution is symmetric with respect to its crest, that is, $\Phi_s(x,z) - \Phi_s(0,z)$ is odd and $\eta_s(x)$ is even in x with the origin $x = 0$ being placed on the crest, and the decay of $\partial\Phi_s/\partial x$, $\partial\Phi_s/\partial z$ and η_s as $x \to \pm\infty$ is exponentially fast (some of these properties were rigorously proved by Amick & Toland 1981 and Craig & Sternberg 1988).

Now we make a linear stability analysis of the solitary wave on the basis of (2.1)–(2.4). The following form is assumed for the solution of (2.1)–(2.4):

$$\phi = -vx + \Phi_s + \hat{\phi}(x,z)\exp(\lambda t + \mathrm{i}\varepsilon y), \tag{2.7a}$$

$$\eta = \eta_s + \hat{\eta}(x)\exp(\lambda t + \mathrm{i}\varepsilon y), \tag{2.7b}$$

where ε is a given non-negative constant, and λ is an unknown complex constant. Substituting (2.7) into (2.1)–(2.4), linearizing with respect to $(\hat{\phi}, \hat{\eta})$, and imposing decaying conditions for $\hat{\phi}$ and $\hat{\eta}$ as $x \to \pm\infty$, we obtain the following set of equations for $(\hat{\phi}, \hat{\eta})$:

$$\frac{\partial^2\hat{\phi}}{\partial x^2} + \frac{\partial^2\hat{\phi}}{\partial z^2} = \varepsilon^2\hat{\phi} \quad \text{for} \quad -1 < z < \eta_s, \tag{2.8}$$

$$L_K[\hat{\phi}, \hat{\eta}] = -\lambda\hat{\eta} \quad \text{at} \quad z = \eta_s, \tag{2.9}$$

$$L_D[\hat{\phi}, \hat{\eta}] = -\lambda\hat{\phi} \quad \text{at} \quad z = \eta_s, \tag{2.10}$$

$$\frac{\partial\hat{\phi}}{\partial z} = 0 \quad \text{at} \quad z = -1, \tag{2.11}$$

$$\hat{\phi}(x,z) \to 0, \hat{\eta}(x) \to 0 \quad \text{as} \quad x \to \pm\infty, \tag{2.12}$$

where L_K and L_D are linear operators defined by

$$L_K[\hat{\phi}, \hat{\eta}] = \left(-\frac{\partial}{\partial z} + \frac{\mathrm{d}\eta_s}{\mathrm{d}x}\frac{\partial}{\partial x}\right)\hat{\phi} + \left[\frac{\partial^2\Phi_s}{\partial x^2} + \frac{\partial^2\Phi_s}{\partial x\partial z}\frac{\mathrm{d}\eta_s}{\mathrm{d}x} + \left(-v + \frac{\partial\Phi_s}{\partial x}\right)\frac{\mathrm{d}}{\mathrm{d}x}\right]\hat{\eta}, \tag{2.13a}$$

$$L_D[\hat{\phi}, \hat{\eta}] = \left[\left(-v + \frac{\partial\Phi_s}{\partial x}\right)\frac{\partial}{\partial x} + \frac{\partial\Phi_s}{\partial z}\frac{\partial}{\partial z}\right]\hat{\phi} + \left[\left(-v + \frac{\partial\Phi_s}{\partial x}\right)\frac{\partial^2\Phi_s}{\partial x\partial z} + \frac{\partial\Phi_s}{\partial z}\frac{\partial^2\Phi_s}{\partial z^2} + 1\right]\hat{\eta}. \tag{2.13b}$$

Equations (2.8)–(2.12) constitute an eigenvalue problem for $(\hat{\phi}, \hat{\eta})$, whose eigenvalue is λ. When this problem possesses a solution for which λ has a positive real part, the solitary wave is linearly unstable to a disturbance of transverse wavenumber ε. In prior studies, the longitudinal stability, or the stability with respect to disturbances that have no dependence on y ($\varepsilon = 0$), was examined numerically by Tanaka (1986) and Longuet-Higgins & Tanaka (1997). According to them, surface solitary waves are longitudinally stable if

$$h < 0.7807, \tag{2.14}$$

where h is defined by (2.6). This critical amplitude $h = 0.7807$ corresponds to the first

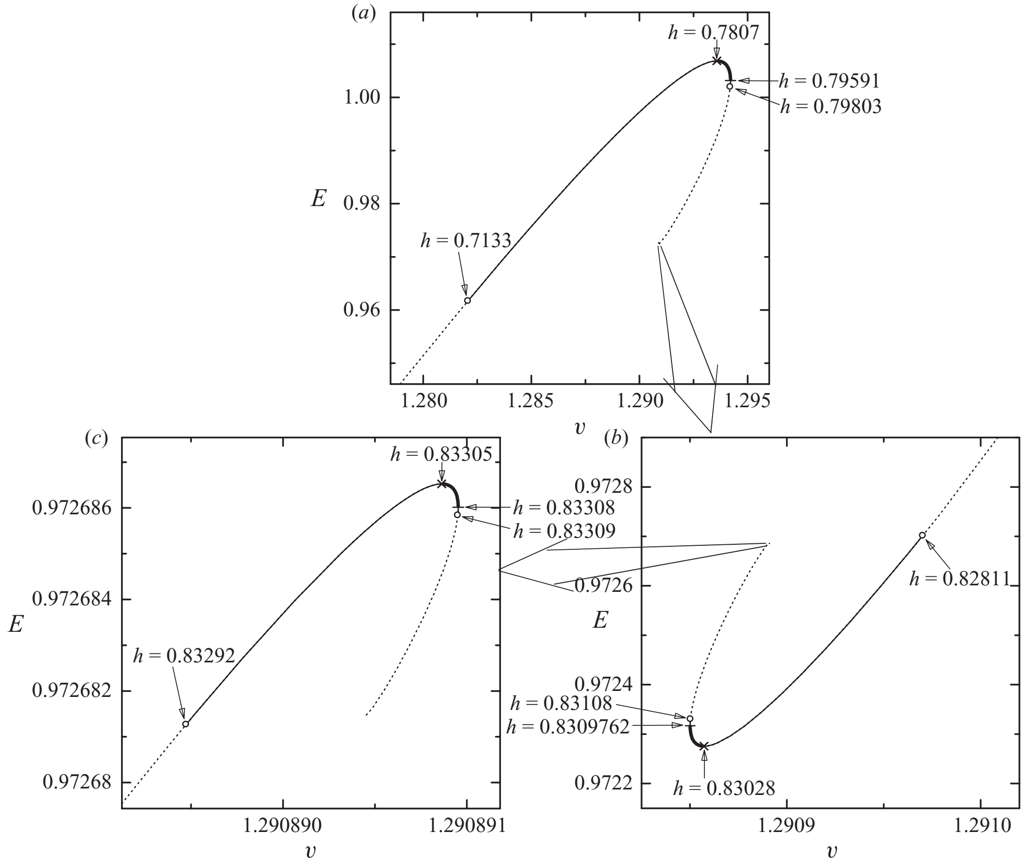

FIGURE 1. Energy E versus wave speed v of the solitary wave as the wave amplitude h increases: (a) whole view; (b) enlarged view at the higher-amplitude end of (a); (c) further enlarged view at the higher-amplitude end of (b). The dotted line represents the range of $\mathrm{d}E/\mathrm{d}v > 0$ and $Q > 0$, the thin solid line that of $\mathrm{d}E/\mathrm{d}v > 0$ and $Q < 0$, and the thick solid line that of $\mathrm{d}E/\mathrm{d}v < 0$ (always $Q < 0$). The crosses, the circles and the short horizontal lines denote the points of $\mathrm{d}E/\mathrm{d}v = 0$, $Q = 0$ and $\mathrm{d}v/\mathrm{d}h = 0$, respectively, for which the corresponding wave amplitudes h are shown in the figure.

extremum in the energy E of the solitary wave defined by

$$E = \frac{1}{2}\int_{-\infty}^{\infty}\left\{\int_{-1}^{\eta_s}\left[\left(\frac{\partial \Phi_s}{\partial x}\right)^2 + \left(\frac{\partial \Phi_s}{\partial z}\right)^2\right]\mathrm{d}z + \eta_s^2\right\}\mathrm{d}x. \tag{2.15}$$

It was then proved by Kataoka (2006a) that an exchange of longitudinal stabilities occurs at every extremum in E. The profile of E is shown as a function of v in figure 1. The points of extrema in E are denoted by the crosses and the corresponding wave amplitudes by $h = 0.7807, 0.83028, 0.83305, \ldots$ in figure 1. The number of unstable modes increases by one after passing through each cross along the solution branch in the direction of increasing h. Thus, the solitary wave is unstable to a single longitudinal mode for $0.7807 < h < 0.83028$, and two modes for $0.83028 < h < 0.83305$.

As for the transverse stability, or the stability to disturbances that depend not only on the x and z directions but also on the y direction ($\varepsilon > 0$), Kataoka & Tsutahara

(2004*a*) and Kataoka (2008) performed an asymptotic analysis of (2.8)–(2.12) for small ε and obtained the following solution of the eigenvalues having non-zero real part:

$$\lambda = \begin{cases} \pm\left(\varepsilon\sqrt{\dfrac{-vE}{\mathrm{d}E/\mathrm{d}v}} - \varepsilon^2 Q\right) \quad \text{for} \quad \dfrac{\mathrm{d}E}{\mathrm{d}v} < 0 \text{ (always } Q < 0), & (2.16a) \\ \pm\varepsilon^2 Q \pm \mathrm{i}\varepsilon\sqrt{\dfrac{vE}{\mathrm{d}E/\mathrm{d}v}} \quad \text{for} \quad \dfrac{\mathrm{d}E}{\mathrm{d}v} > 0 \quad \text{and} \quad Q < 0, & (2.16b) \\ \text{no eigenvalue having non-zero real part} \quad \text{for} \quad \dfrac{\mathrm{d}E}{\mathrm{d}v} > 0 \quad \text{and} \quad Q > 0, & (2.16c) \end{cases}$$

where

$$Q = \frac{v^2 E}{2(\mathrm{d}E/\mathrm{d}v)^2}\left(\frac{\mathrm{d}M}{\mathrm{d}v} - \frac{M}{E}\frac{\mathrm{d}E}{\mathrm{d}v}\right)\frac{\mathrm{d}\varOmega}{\mathrm{d}v}, \tag{2.17}$$

and

$$\varOmega = \frac{2T}{v} - vM, \quad M = \int_{-\infty}^{\infty} \eta_s \,\mathrm{d}x, \quad T = \int_{-\infty}^{\infty} \mathrm{d}x \int_{-1}^{\eta_s} \frac{1}{2}\left[\left(\frac{\partial \varPhi_s}{\partial x}\right)^2 + \left(\frac{\partial \varPhi_s}{\partial z}\right)^2\right] \mathrm{d}z \tag{2.18}$$

in which M and T represent, respectively, the mass and the kinetic energy of the solitary wave. The above result (2.16) for λ leads to the following sufficient condition for the transverse instability:

$$Q < 0. \tag{2.19}$$

The range of $Q < 0$ is shown in figure 1 by (either thin or thick) solid lines whose end points are denoted by circles. However, the above eigenvalues (2.16), which lead to (2.19), are valid only for small ε. Thus, in the present study, we will clarify the transverse stability of surface solitary waves for the whole range of ε by solving the eigenvalue problem (2.8)–(2.12) numerically. The numerical method is described in § 3, and the results in §§ 4 and 5.

3. Numerical method

Solitary wave solutions ($\varPhi_s$, η_s) are computed numerically by the method described in Turner & Vanden-Broeck (1988). This method was originally devised for computing interfacial solitary waves in a two-layer fluid. Surface solitary wave solutions are obtained simply by setting the density of the upper fluid to zero – the reader is referred to that paper for details of the numerical method. Convergence of the computed results is so fast that the surface elevation η_s converges up to $O(10^{-7})$ or more on a pointwise basis.

Computation of the eigenvalue problem (2.8)–(2.12) is carried out in the following way. First we introduce Green's function G of the modified Helmholtz equation which satisfies $(\partial^2/\partial x^2 + \partial^2/\partial z^2 - \varepsilon^2)G = -2\pi\delta(x - x', z - z')$ (δ is Dirac's delta function) and an impermeable boundary condition $\partial G/\partial z = 0$ at the bottom $z = -1$, i.e.

$$G(x, z, x', z') = K_0(\varepsilon r) + K_0(\varepsilon \bar{r}), \tag{3.1}$$

where K_0 is the modified Bessel function of the second kind of order zero and

$$r = \sqrt{(x - x')^2 + (z - z')^2}, \quad \bar{r} = \sqrt{(x - x')^2 + (z + z' + 2)^2}. \tag{3.2}$$

Let $\hat{\phi}(x,z)$ be defined by

$$\hat{\phi}(x,z)=\int_{-\infty}^{\infty}\sigma(s')G(x,z,x'(s'),z'(s'))\,\mathrm{d}s', \tag{3.3}$$

where s is the arc length along the surface $z=\eta_s$ of the solitary wave measured from the crest at $x=0$, $\sigma(s)$ is an unknown function of s, and $(x(s),z(s))$ is the space coordinate on the surface of the solitary wave. The spatial derivatives of $\hat{\phi}$ along the surface and normal to it evaluated on the surface $(x,z)=(x(s),z(s))$ are expressed as

$$\frac{\partial\hat{\phi}}{\partial s}=PV\int_{-\infty}^{\infty}\sigma(s')\frac{\partial G}{\partial s}\,\mathrm{d}s',\quad \frac{\partial\hat{\phi}}{\partial n}=\pi\sigma+\int_{-\infty}^{\infty}\sigma(s')\frac{\partial G}{\partial n}\,\mathrm{d}s', \tag{3.4a,b}$$

where PV denotes principal value, and n is the normal to the surface, pointing out of the fluid. The eigenvalue problem (2.8)–(2.12) for $\hat{\phi}(x,z)$ and $\hat{\eta}(x)$ then reduces to that of integro-differential equations for $\hat{\eta}(s)$ and $\sigma(s)$ evaluated on the surface $(x,z)=(x(s),z(s))$:

$$\lambda\hat{\eta}=\frac{1}{\cos\theta}\left[\pi\sigma+\int_{-\infty}^{\infty}\sigma(s')\frac{\partial G}{\partial n}\,\mathrm{d}s'+\frac{\mathrm{d}(q\cos\theta\hat{\eta})}{\mathrm{d}s}\right], \tag{3.5}$$

$$\lambda\int_{-\infty}^{\infty}\sigma(s')G\mathrm{d}s'=q\times PV\int_{-\infty}^{\infty}\sigma(s')\frac{\partial G}{\partial s}\,\mathrm{d}s'-\left[q\frac{\mathrm{d}(q\sin\theta)}{\mathrm{d}s}+1\right]\hat{\eta}, \tag{3.6}$$

with boundary conditions

$$\hat{\eta}(s)\rightarrow 0,\quad \sigma(s)\rightarrow 0\quad \text{as}\quad s\rightarrow\pm\infty, \tag{3.7}$$

where $q(s)$ and $\theta(s)$ are, respectively, the flow speed of the solitary wave on the surface $(x,z)=(x(s),z(s))$ and the angle between the s-axis and x-axis, i.e.

$$q(s)=\left[\left(-v+\frac{\partial\Phi_s}{\partial x}\right)^2+\left(\frac{\partial\Phi_s}{\partial z}\right)^2\right]^{1/2}_{(x,z)=(x(s),z(s))},\quad \theta(s)=\arctan\left(\frac{\mathrm{d}\eta_s}{\mathrm{d}x}\right). \tag{3.8a,b}$$

To solve the eigenvalue problem (3.5)–(3.7) numerically, we employ the following new independent variable γ:

$$s(\gamma)=\Delta_{min}\gamma+(\Delta_{max}-\Delta_{min})\int_0^{\gamma}\tanh^8\left(\frac{\Delta_{max}\gamma'}{L}\right)\mathrm{d}\gamma', \tag{3.9}$$

where Δ_{min}, Δ_{max} $(>\Delta_{min})$ and L are positive constants. The $2N+1$ discrete mesh points are distributed at $\gamma_i=i/N$ $(i=-N,-N+1,\ldots,N)$. Introduction of the above coordinate γ enables us to concentrate these mesh points towards the origin $s=0$ with a minimum width Δ_{min}/N, while they are distributed almost equally with a moderate width Δ_{max}/N in the far field. Thus, we can capture both a steep variation of the solution near the solitary-wave crest and a moderate variation in the far field with high accuracy by choosing Δ_{min} and Δ_{max} appropriately.

The two integrals $PV\int_{-\infty}^{\infty}\sigma(s')\partial G/\partial s\,\mathrm{d}s'$ and $\int_{-\infty}^{\infty}\sigma(s')G\,\mathrm{d}s'$ in (3.6) contain an inverse-first-power singularity and a logarithmic singularity, respectively. To calculate these integrals, we introduce a new set of mesh points $\gamma_{i-1/2}=(i-1/2)/N$. The former integral is calculated by the usual trapezoidal rule by evaluating the variables with s and those with s' at different sets of mesh points $\gamma_{i-1/2}$ and γ_i, respectively. The latter integral is first divided into a singular part $-\int_{s(\gamma_{i-2})}^{s(\gamma_{i+1})}\sigma(s')\ln|s'-s(\gamma_{i-1/2})|\mathrm{d}s'$ and the remaining non-singular part, and $\sigma(s')$ in the singular part is approximated by a cubic

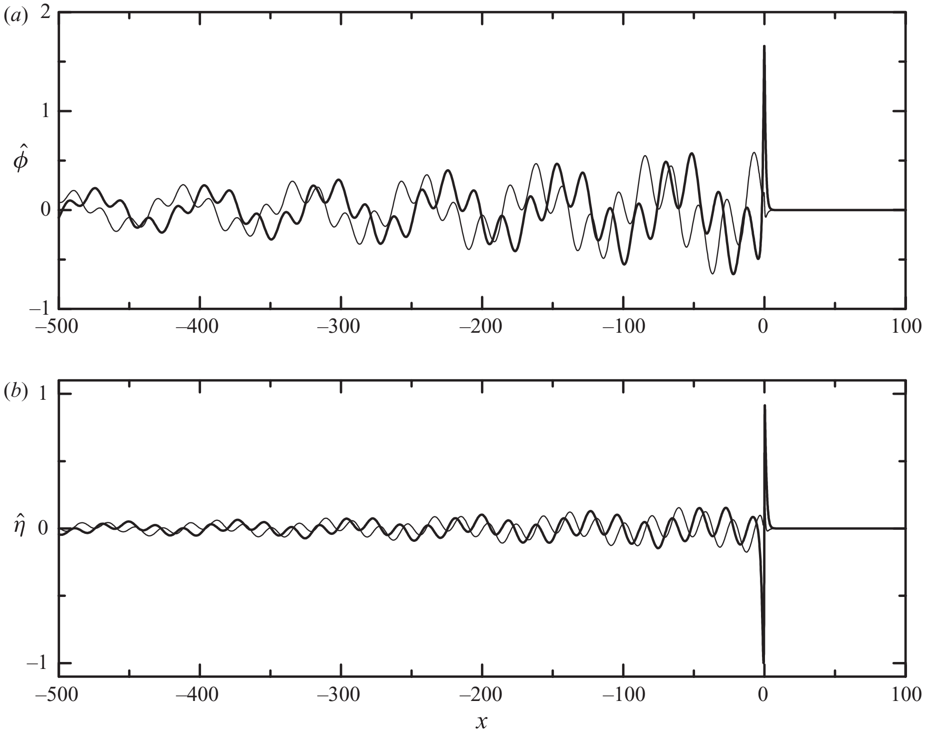

FIGURE 2. Eigenfunctions $(\hat{\phi}, \hat{\eta})$ of a growing disturbance mode for $(h, \varepsilon) = (0.76, 0.15)$. The thick and thin solid lines represent the real and imaginary parts, respectively, under the normalization (5.1).

function of s' as

$$\sigma(s') = a_3 s'^3 + a_2 s'^2 + a_1 s' + a_0, \tag{3.10}$$

where the coefficients a_0, a_1, a_2 and a_3 are determined by evaluation of (3.10) at four discrete mesh points $s' = s(\gamma_{i-2})$, $s(\gamma_{i-1})$, $s(\gamma_i)$ and $s(\gamma_{i+1})$. The non-singular part is computed by the usual Simpson's rule. Finally, evaluating the derivative $\mathrm{d}\hat{\eta}/\mathrm{d}s$ in (3.5) by the four-point centred finite-difference formula and expressing the boundary condition (3.7) as $\hat{\eta}(\gamma_j) = \sigma(\gamma_j) = 0$ for $|j| \geqslant N + 1$, we obtain the following $4N + 2$ algebraic equations for $\{\hat{\eta}, \sigma\} \equiv (\hat{\eta}(\gamma_{-N}), \hat{\eta}(\gamma_{-N+1}), \ldots, \hat{\eta}(\gamma_N), \sigma(\gamma_{-N}), \sigma(\gamma_{-N+1}), \ldots, \sigma(\gamma_N))$ from (3.5) and (3.6):

$$\lambda\, [\boldsymbol{Y}] \begin{Bmatrix} \hat{\eta} \\ \sigma \end{Bmatrix} = [\boldsymbol{Z}] \begin{Bmatrix} \hat{\eta} \\ \sigma \end{Bmatrix}, \tag{3.11}$$

where $[\boldsymbol{Y}]$ and $[\boldsymbol{Z}]$ are the linear operators of $(4N + 2) \times (4N + 2)$ matrix form. Now the original eigenvalue problem (2.8)–(2.12) reduces to that of the $4N + 2$ algebraic equations (3.11). The eigenvalues λ of the $(4N + 2) \times (4N + 2)$ matrix $[\boldsymbol{Y}^{-1}\boldsymbol{Z}]$ are obtained by the QR algorithm (Wilkinson 1965).

Figure 2 shows computed eigenfunctions $(\hat{\phi}, \hat{\eta})$ of a growing disturbance mode for $(h, \varepsilon) = (0.76, 0.15)$ (under the normalization (5.1) below). We see that the decay of the eigenfunctions as $x \to -\infty$ is very slow. Since the eigenfunctions make oscillations while they decay slowly as $x \to -\infty$, we need an enormous number of mesh points in order to extend the computational domain up to the x-coordinate where the

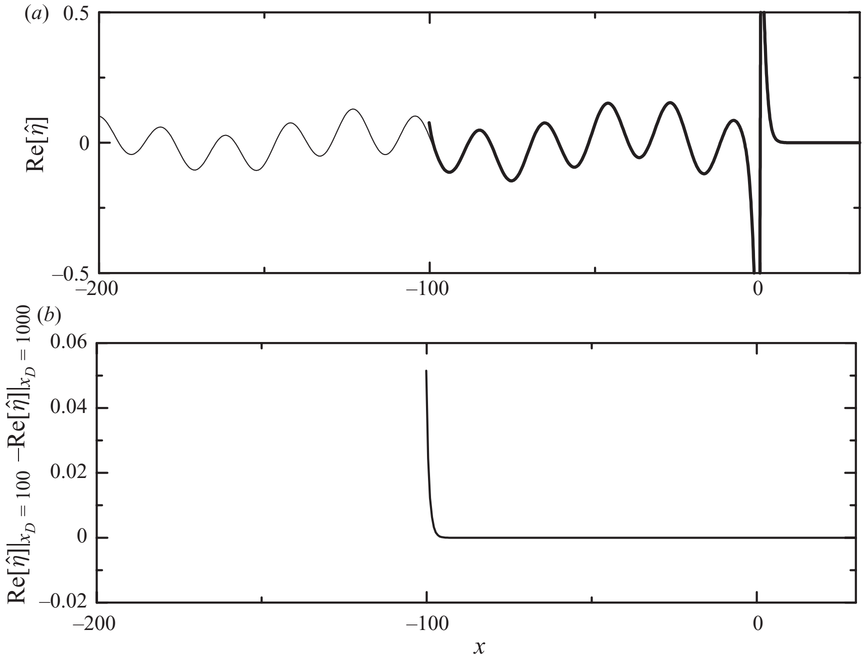

FIGURE 3. Real parts Re[$\hat{\eta}$] of computed eigenfunction $\hat{\eta}$ for two different values of $x_D = 100$ (thick solid line) and 1000 (thin solid line) when $(h, \varepsilon) = (0.76, 0.15)$ (shown in (*a*)). Their difference $\mathrm{Re}[\hat{\eta}]|_{x_D=100} - \mathrm{Re}[\hat{\eta}]|_{x_D=1000}$ is shown in (*b*).

eigenfunctions completely decay. Especially when the speed of decay is much slower, it is impossible to perform the computation within a reasonable time and memory size. Thus, we tried to set the downstream end of the computational domain on the x-coordinate where the eigenfunctions do not completely decay ($\hat{\eta} = \sigma = 0$ is imposed outside the computational domain), and carefully see how this artificial boundary put on non-zero eigenfunctions influences the convergence of the numerical results for various sets of (h, ε). The numerical results show very fast convergence of the computed eigenvalues λ in terms of x_D, where $-x_D$ (which is almost equal to (3.9) with $\gamma = -1$) is the x-coordinate of the downstream artificial boundary. Specifically, convergence of λ in terms of x_D is achieved up to $O(10^{-7})$ or more with only $x_D \geqslant 30$. The real parts of the computed eigenfunction $\hat{\eta}$ for two different values of x_D (=100 and 1000) and their difference are also shown in figure 3, and we see that the error is induced only in the vicinity of the artificial boundary (the same is true of their imaginary parts and the other eigenfunction $\hat{\phi}$). Thus, the numerical results are scarcely influenced by the artificial boundary put on non-zero eigenfunctions.

Next, we examine convergence in terms of the mesh width. Table 1 shows convergence of computed eigenvalues λ as half the number N of mesh points is increased for other given computational parameters. We see that convergence up to three significant digits is achieved with $N = 800$ and 400 from the results for $(h, \varepsilon) = (0.76, 0.15)$ and (0.830976, 0.13), respectively. In the present study we sought convergence up to at least three and two significant digits for any computed eigenvalues λ of $\mathrm{Re}[\lambda] \geqslant 10^{-3}$ and $\mathrm{Re}[\lambda] < 10^{-3}$, respectively.

	(*a*)	(*b*)		
N	λ	λ (complex)	λ (smaller real)	λ (larger real)
200	0.0014879 ± 0.069577 i	0.011209 ± 0.028118 i	0.0048662	0.92000
400	0.0015007 ± 0.069583 i	0.011260 ± 0.028094 i	0.0048043	0.92079
800	0.0015054 ± 0.069586 i	0.011268 ± 0.028080 i	0.0048010	0.92102
1600	0.0015075 ± 0.069587 i	0.011271 ± 0.028074 i	0.0048018	0.92110

TABLE 1. Convergence of computed eigenvalues λ as half the number N of mesh points is increased: (*a*) $(h, \varepsilon) = (0.76, 0.15)$; (*b*) $(h, \varepsilon) = (0.830976, 0.13)$. The computational parameters are chosen as $(\Delta_{min}, \Delta_{max}, L) = (0.6, 250, 90)$ and $(0.06, 250, 90)$ for (*a*) and (*b*), respectively. $x_D = 102$ for both cases.

4. Eigenvalues

Surface solitary waves are longitudinally stable for $h < 0.7807$, and longitudinally unstable to a single disturbance mode for $0.7807 < h < 0.83028$ and two modes for $0.83028 < h < 0.83305$ (see the discussion after (2.15)). Numerical results of eigenvalues obtained from linear stability analysis are given here in separate subsections for three different types of solitary waves: longitudinally stable ones in § 4.1, those longitudinally unstable to a single mode in § 4.2, and those longitudinally unstable to two modes in § 4.3. The transverse instabilities presented in these three subsections are then classified in § 4.4.

4.1. *Longitudinally stable solitary waves* ($h < 0.7807$)

Numerical computation is carried out for various sets of $h(<0.7807)$ and ε. Calculation is made at least every 0.02 and 0.5 in ε in the ranges of $\varepsilon \leqslant 1$ and $1 < \varepsilon \leqslant 20$, respectively. For $h \leqslant 0.713$, there is no eigenvalue with a positive real part (in the range of $\varepsilon \leqslant 20$). For $h \geqslant 0.714$, on the other hand, there is a single pair of complex-conjugate eigenvalues with a positive real part if ε is sufficiently small and non-zero. This result is consistent with the theoretical result obtained by Kataoka & Tsutahara (2004*a*) that the solitary wave is transversely unstable for $h > 0.7133$. The real part $\mathrm{Re}[\lambda]$ of the above computed eigenvalues having a positive real part is plotted as a function of ε for $h = 0.714$, 0.716, 0.718 and 0.72 in figure 4, and for $h = 0.74$, 0.76 and 0.78 in figure 5(*a*). The dashed line is the asymptotic solution for small ε given by (2.16*b*), which agrees well with the corresponding numerical result for small ε when $h \leqslant 0.76$ (for $\varepsilon \leqslant 0.02$ when $h \leqslant 0.72$ and for $\varepsilon \leqslant 0.03$ when $0.74 \leqslant h \leqslant 0.76$), whereas agreement is poor for $h = 0.78$. The large deviation for $h = 0.78$ is due to the fact that the asymptotic solution (2.16) does not give good approximation near the longitudinal stability threshold $h = 0.7807$, where $|\mathrm{d}E/\mathrm{d}v|$ is small (see figure 1). The asymptotic analysis that takes into account the effect of small $|\mathrm{d}E/\mathrm{d}v|$ is carried out in Appendix A, and the result (A 25*b*) for $h = 0.78$ is plotted in figure 5(*a*) in the solid line. Good agreement with the numerical result is achieved.

Figures 4 and 5(*a*) show that the growth rate $\mathrm{Re}[\lambda]$, which is an increasing function of ε for small ε, reaches a peak $\mathrm{Re}[\lambda]_{max}$ at some finite wavenumber $\varepsilon = \varepsilon_{peak}$ (peak wavenumber) and finally falls to zero at the higher wavenumber $\varepsilon = \varepsilon_C$ (cutoff wavenumber). This result implies that there is a high-wavenumber cutoff to the transverse instability: the solitary wave is transversely unstable to a disturbance of $\varepsilon < \varepsilon_C$, and stable to that of $\varepsilon > \varepsilon_C$. Table 2 arranges the maximum growth rate $\mathrm{Re}[\lambda]_{max}$, the peak wavenumber ε_{peak} at which $\mathrm{Re}[\lambda]_{max}$ is achieved and the cutoff wavenumber ε_C at which $\mathrm{Re}[\lambda]$ falls to zero, for various values of h (<0.7807).

h	$\mathrm{Re}[\lambda]_{max}$	ε_{peak}	ε_C	Class of instability
0.714	5×10^{-7}	0.011	0.016	C_0
0.716	9×10^{-6}	0.023	0.033	
0.718	2.6×10^{-5}	0.030	0.044	
0.72	5.5×10^{-5}	0.036	0.053	
0.73	3.8×10^{-4}	0.057	0.087	
0.74	1.09×10^{-3}	0.072	0.114	
0.75	2.35×10^{-3}	0.083	0.140	
0.76	4.40×10^{-3}	0.091	0.164	
0.77	7.60×10^{-3}	0.093	0.187	
0.78	0.0126	0.0884	0.205	
0.7806	0.0130	0.0877	0.206	

TABLE 2. Maximum growth rate $\mathrm{Re}[\lambda]_{max}$, peak wavenumber ε_{peak} at which $\mathrm{Re}[\lambda]_{max}$ is achieved, and cutoff wavenumber ε_C at which $\mathrm{Re}[\lambda]$ falls to zero, when the solitary wave is longitudinally stable but transversely unstable ($0.7133 < h < 0.7807$). See §4.4 for the class of instability and figure 15(b) for the typical profile of $\mathrm{Re}[\lambda]$ versus ε.

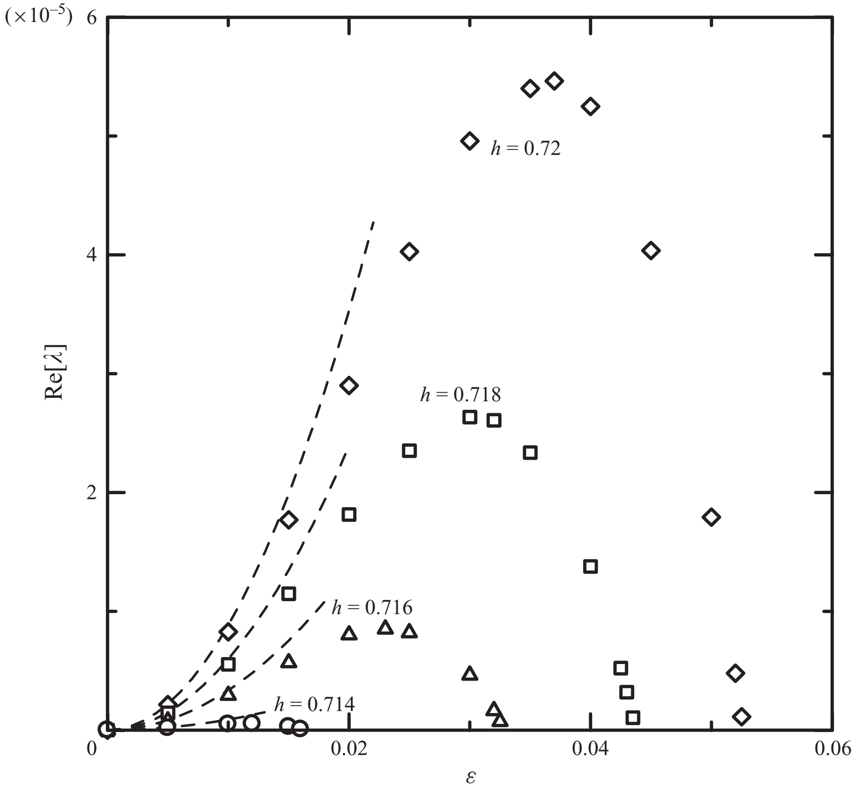

FIGURE 4. Real parts $\mathrm{Re}[\lambda]$ of computed eigenvalues λ having a positive real part versus ε for $h = 0.714$ (○), 0.716 (△), 0.718 (□) and 0.72 (◇). The dashed line represents the asymptotic solution (2.16) for small ε.

We find that ε_{peak} has a maximum at $h = 0.770$, whereas ε_C is a monotonically increasing function of h for the longitudinally stable and transversely unstable range $0.7133 < h < 0.7807$.

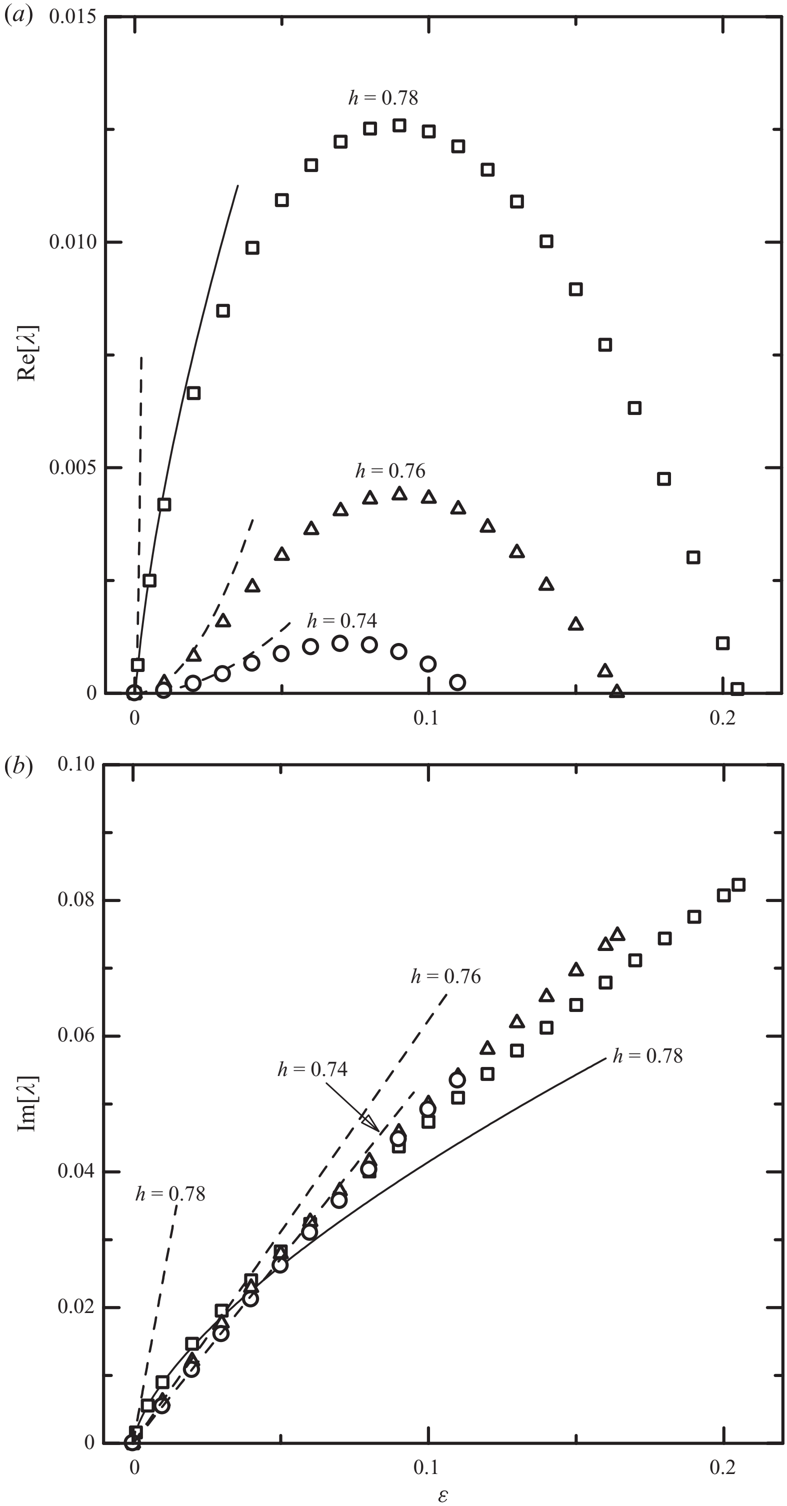

FIGURE 5. Computed eigenvalues λ with a positive real part versus ε for $h = 0.74$ (○), 0.76 (△), and 0.78 (□): (*a*) Re[λ] versus ε; (*b*) Im[λ] versus ε. See caption of figure 4 for the dashed line. The solid line for $h = 0.78$ is the asymptotic solution (A 25*b*) that takes into account the effect of small $|\mathrm{d}E/\mathrm{d}v|$.

h	ε_{merge}	ε_S	ε_L	ε_C	ε_{R1}	Class of instability
0.785	0.006	–	–	0.211	–	R_0
0.79	0.025	–	–	0.209	–	
0.795	0.072	–	–	0.184	–	
0.7952	0.076	0.24	0.33	0.182	–	R_1
0.7958	0.091	0.070	0.45	0.174	–	
0.7959	0.095	0.020	0.46	0.172	–	R_2
0.79595	–	–	–	0.172	0.47	C_1
0.796	–	–	–	0.171	0.47	C_0
0.797	–	–	–	0.147	0.56	
0.798	–	–	–	0.054	0.64	
0.7981	–	–	–	–	0.65	N
0.8	–	–	–	–	0.78	
0.81	–	–	–	–	1.5	
0.82	–	–	–	–	3.3	
0.828	–	–	–	–	10	
0.829	–	–	–	0.132	13	C_0
0.83	–	–	–	0.198	17	

TABLE 3. Merging wavenumber ε_{merge} of two real branches starting from $\varepsilon = 0$, smaller- and larger-end wavenumbers ε_S and ε_L of arc-shaped real branch, and cutoff wavenumbers ε_C and ε_{R1} of complex and the first real branches of eigenvalues, respectively, when the solitary wave is unstable to a single longitudinal disturbance mode ($0.7807 < h < 0.83028$). See §4.4 for the class of instability and figure 15 for typical profiles of Re[λ] versus ε.

The imaginary part Im[λ] of the above complex-conjugate eigenvalues with a positive real part is plotted for $h = 0.74$, 0.76 and 0.78 in figure 5(*b*) (Im[λ] is taken to be positive). The dashed line is the asymptotic solution (2.16*b*) for small ε, which agrees well with the numerical result for small ε for $h \leqslant 0.76$, whereas agreement is poor for $h = 0.78$ due to the above-mentioned reason that (2.16) does not give a good approximation for small $|\mathrm{d}E/\mathrm{d}v|$. The asymptotic solution (A 25*b*) that takes into account the effect of small $|\mathrm{d}E/\mathrm{d}v|$ is shown by the solid line in figure 5(*b*) for $h = 0.78$, which agrees well with the corresponding numerical result for small ε. As ε increases, Im[λ] continues to rise until the cutoff wavenumber $\varepsilon = \varepsilon_C$, whereas Re[$\lambda$] reaches an upper limit and then falls to zero at $\varepsilon = \varepsilon_C$.

4.2. *Solitary waves longitudinally unstable to a single mode* ($0.7807 < h < 0.83028$)

As in §4.1, we computed at least every 0.02 and 0.5 in ε in the ranges of $\varepsilon \leqslant 1$ and $1 < \varepsilon \leqslant 20$, respectively. Eigenvalues λ with a positive real part versus ε thus obtained are plotted in figure 6 for $h = 0.785$, 0.79 and 0.795. In contrast to the longitudinally stable case where the eigenvalues are all complex, there are real eigenvalues (represented by the black circles in figure 6). The dashed line in figure 6(*a*) is the asymptotic solution (2.16*a*) for small ε, which agrees well with the corresponding numerical result for sufficiently small ε and $|\lambda|$. There are two branches of real eigenvalues for a given ε: one starting from $\lambda > 0$ at $\varepsilon = 0$ and the other from the origin. These two real branches merge at some wavenumber $\varepsilon = \varepsilon_{merge}$ (merging wavenumber), becoming a single branch of complex-conjugate eigenvalues with a positive real part (represented by the white circles in figure 6). This complex branch extends to its cutoff wavenumber $\varepsilon = \varepsilon_C$. Specific values of ε_{merge} and ε_C are tabulated in table 3.

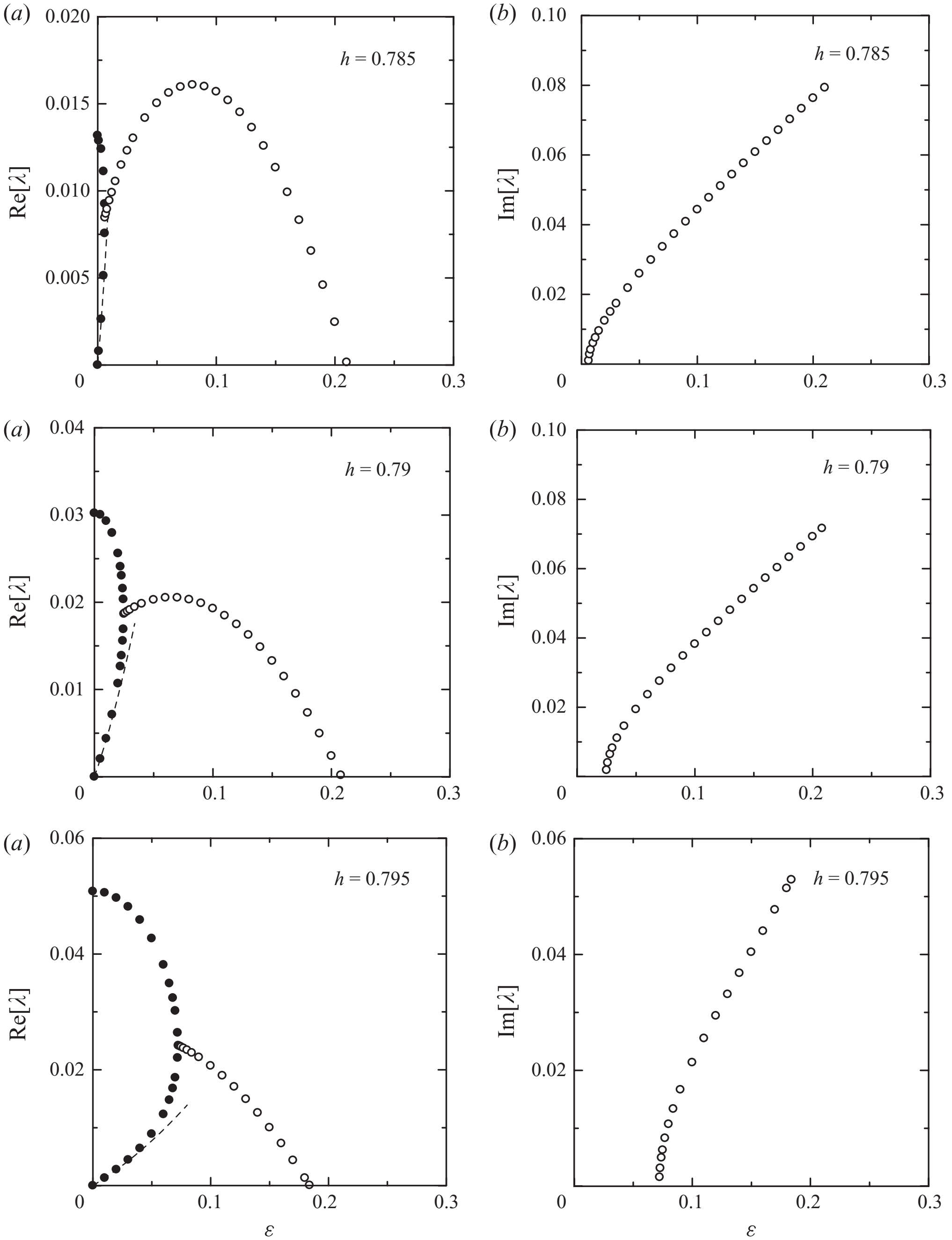

FIGURE 6. Computed eigenvalues λ with a positive real part versus ε for $h = 0.785$, 0.79 and 0.795: (*a*) Re[λ] versus ε; (*b*) Im[λ] versus ε. ● and ○ denote numerical results for the real and complex eigenvalues, respectively. See caption of figure 4 for the dashed line.

Figure 6(*a*) indicates that the maximum growth rate $\mathrm{Re}[\lambda]_{max}$ is achieved by a transverse disturbance ($\varepsilon > 0$) for $h \leqslant 0.785$ but by a longitudinal one ($\varepsilon = 0$) for $h \geqslant 0.79$. The most rapidly growing disturbance mode switches from the transverse

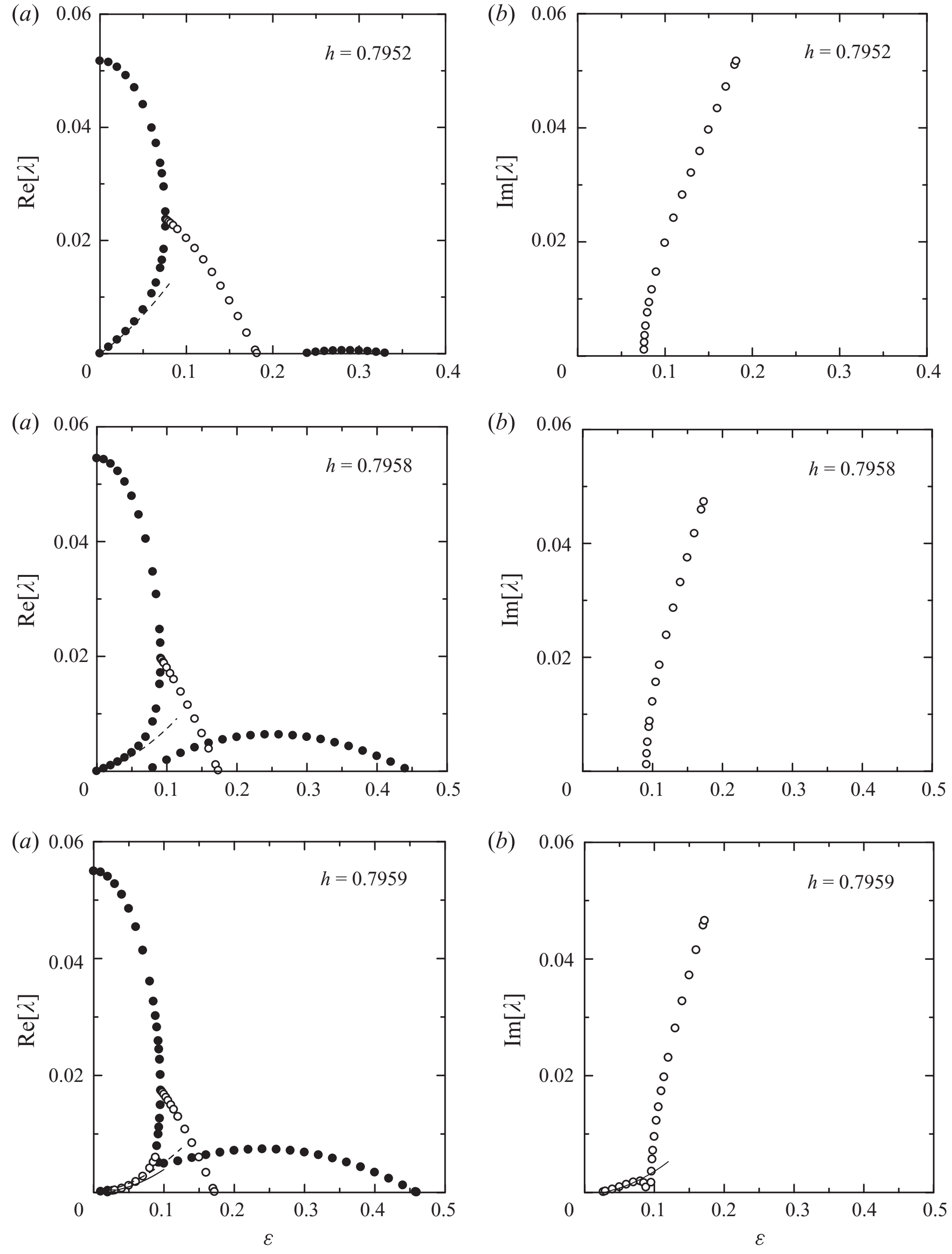

FIGURE 7. For caption see page 142.

(three-dimensional) one to the longitudinal (two-dimensional) one when h is between 0.785 and 0.79, or more precisely, between 0.7863 and 0.7864.

Figure 7 shows λ versus ε for $h = 0.7952$, 0.7958, 0.7959, 0.79595, 0.796 and 0.797. The dashed line is the asymptotic solution (2.16) for small ε, and good agreement with the numerical result is achieved up to around $\varepsilon = 0.05$, except for the case

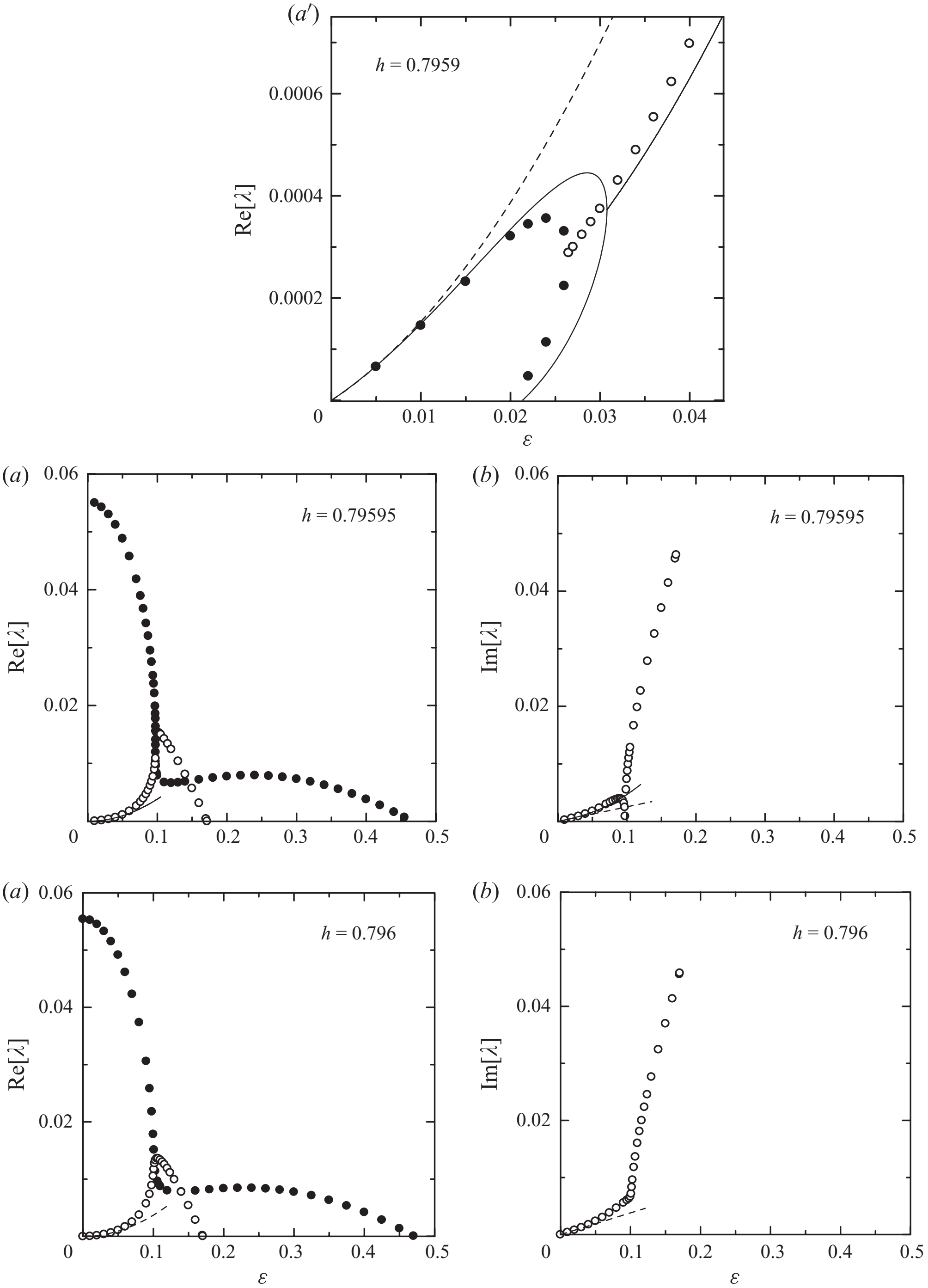

FIGURE 7. For caption see page 142.

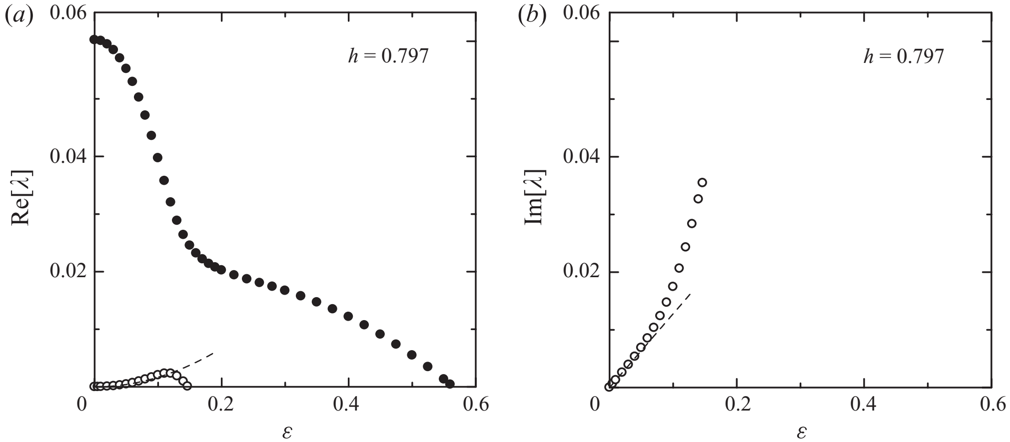

FIGURE 7. Computed eigenvalues λ with a positive real part versus ε for $h = 0.7952$, 0.7958, 0.7959, 0.79595, 0.796 and 0.797: (*a*) Re[λ] versus ε; (a') enlarged view of (*a*) for $h = 0.7959$ near the origin; (*b*) Im[λ] versus ε; ● and ○ denote numerical results for the real and complex eigenvalues, respectively. See caption of figure 4 for the dashed line. The solid line for $h = 0.7959$ and 0.79595 is the asymptotic solution (B 25) that takes into account the effect of small $|dv/dh|$. Note that the dashed line in (*a*) for $h = 0.79595$ is superposed on the solid line.

of $h = 0.7959$; agreement is poor for $h = 0.7959$, as shown in figure 7(a'). Such a deviation for $h = 0.7959$ is due to the fact that the above asymptotic solution (2.16) does not give a good approximation when $|dv/dh|$ is small ($dv/dh = 0$ at $h = 0.79591$; see figure 1*a*). Asymptotic analysis that takes into account the effect of small $|dv/dh|$ is carried out in Appendix B, and the result (B 25) for $h = 0.7959$ is plotted in the solid line in figure 7. Good agreement with the corresponding numerical result can be found, and a complicated dependence of λ on ε is realized well (see figure 7a'). The same asymptotic solution (B 25) is also plotted for $h = 0.79595$ in the solid line in figure 7, which agrees well with the numerical result for small ε.

Let us see how the profile of λ versus ε varies as h increases around $dv/dh = 0$ (around $h = 0.79591$). For $h = 0.7952$ an arc-shaped branch of real eigenvalues appears from the axis Re[λ] = 0 with both ends placed on the axis Re[λ] = 0 (see figure 7*a* for $h = 0.7952$). The positions of the two ends, denoted by $\varepsilon = \varepsilon_S$ and ε_L ($>\varepsilon_S$), are tabulated in table 3. As h increases further, this arc-shaped branch approaches the pre-existing real branch (see figure 7*a* for $h = 0.7958$), and partly merges with it, forming a single complex branch (see figure 7*a* for $h = 0.7959$). This complex branch extends its range to the origin and the larger-ε side, and finally reaches the origin at $h = 0.79591$ (see figure 7*a* for $h = 0.79595$) and the pre-existing complex branch on the larger-ε side at $h = 0.795955$ (see figure 7*a* for $h = 0.796$). As a result of this process, a unified complex branch and a unified real branch are constructed. Thus, there are two independent unstable branches, the complex one and the real one (the latter is called the first real branch), which run for $0 < \varepsilon < \varepsilon_C$ and $0 < \varepsilon < \varepsilon_{R1}$, respectively. Such examples of λ versus ε are shown in figure 7 for $h = 0.796$ and 0.797. Their cutoff wavenumbers ε_C and ε_{R1} are tabulated in table 3.

As h becomes larger, the above complex branch approaches the axis Re[λ] = 0 (see figure 7*a* for $h = 0.797$), and finally disappears into the axis Re[λ] = 0 at $h = 0.79803$ when Q defined by (2.17) changes sign to positive (see figure 1*a*). Figure 8 clearly shows the complex branch approaching the axis Re[λ] = 0 for $h = 0.7977$, 0.7978,

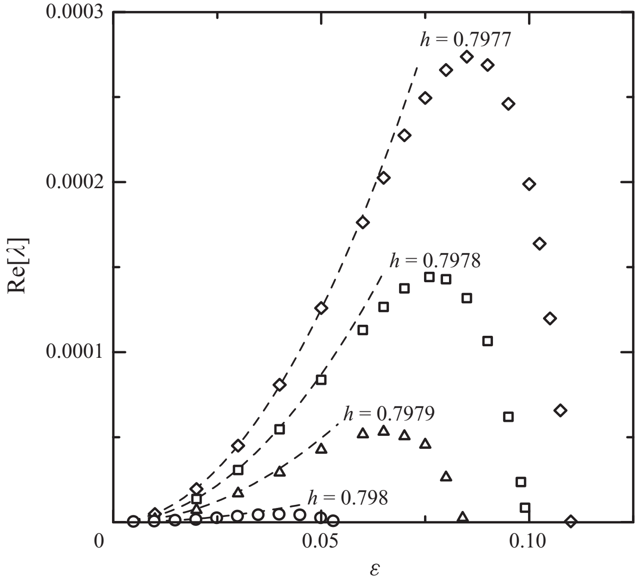

FIGURE 8. Re[λ] versus ε for $h = 0.7977$ (◇), 0.7978 (□), 0.7979 (△) and 0.798 (○). See caption of figure 4 for the dashed line. Note that there is an additional branch of positive real eigenvalues (the first real branch) outside the range of the figure.

0.7979 and 0.798. After disappearance of the complex branch, only the first real branch remains as an unstable branch. Such examples of λ versus ε are presented in figure 9 for $h = 0.7981$, 0.81, 0.82 and 0.828, and their cutoff wavenumbers ε_{R1} are tabulated in table 3.

The complex branch, which disappeared at $h = 0.79803$, reappears from the axis Re[λ] $= 0$ at $h = 0.82811$ when Q becomes negative again (see figure 1*b*). Figure 10 clearly shows such reappearance of the complex branch for $h = 0.8282$, 0.8283 and 0.8284. Figure 11(a') shows the above complex branch for the larger amplitudes $h = 0.829$ and 0.83. The dashed line is the ordinary asymptotic solution (2.16*b*) for small ε, and the solid line for $h = 0.83$ is the solution (A 25*b*) that takes into account the effect of small $|\mathrm{d}E/\mathrm{d}v|$ ($\mathrm{d}E/\mathrm{d}v = 0$ at $h = 0.83028$; see figure 1*b*). The dashed line for $h = 0.829$ and the solid line for $h = 0.83$ agree well with the corresponding numerical results for $\varepsilon \leqslant 0.03$. Figure 11($a$) shows that there is an additional real branch (the first real branch) of large positive eigenvalues. The cutoff wavenumbers ε_C and ε_{R1} of the complex and the first real branches are tabulated in table 3.

It should be noted here that the unstable complex branch appears only when $Q < 0$, and its profile on the ε − Re[λ] plane is similar if the sign of $\mathrm{d}E/\mathrm{d}v$ is the same. For instance, the complex branches for $h = 0.796$, 0.797 (see figure 7*a*), 0.829 and 0.83 (see figure 11*a*′), for which $\mathrm{d}E/\mathrm{d}v > 0$, all start from the origin in such a way that the real part Re[λ] rises to its maximum and falls to zero. In contrast, the complex branches for $h = 0.785$, 0.79, 0.795, 0.7952 and 0.7958 (see figures 6*a* and figures 7*a*), for which $\mathrm{d}E/\mathrm{d}v < 0$, start not from the origin but bifurcate from the middle of the real branch and fall to Re[λ] $= 0$. Such a similarity of Re[λ] versus ε depending on the signs of the two parameters $\mathrm{d}E/\mathrm{d}v$ and Q of the solitary wave will be discussed more generally in § 4.4.

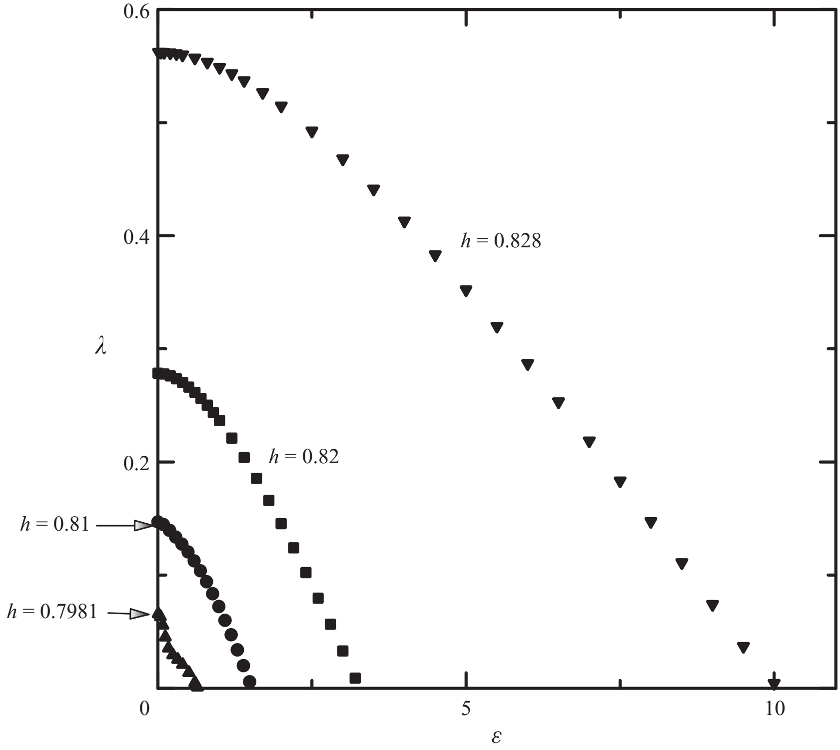

FIGURE 9. Computed eigenvalues λ with a positive real part (which are all real) versus ε for $h = 0.7981$ (▲), 0.81 (●), 0.82 (■) and 0.828 (▼).

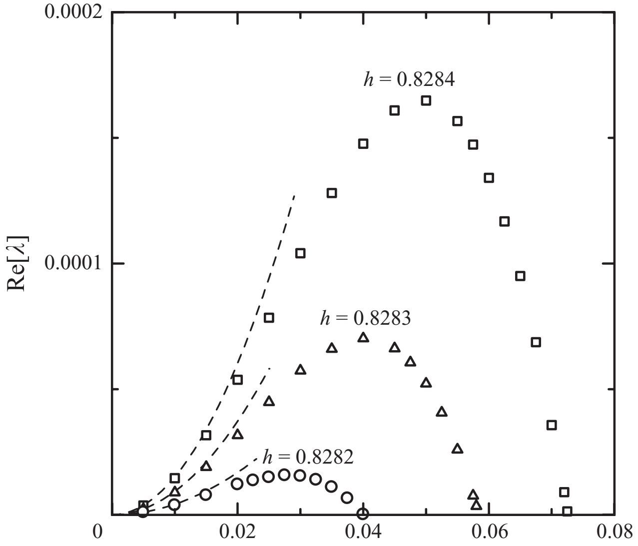

FIGURE 10. Re[λ] versus ε for $h = 0.8282$ (denoted by ○), 0.8283 (△) and 0.8284 (□). See caption of figure 4 for the dashed line. Note that there is an additional branch of positive real eigenvalues outside the range of the figure.

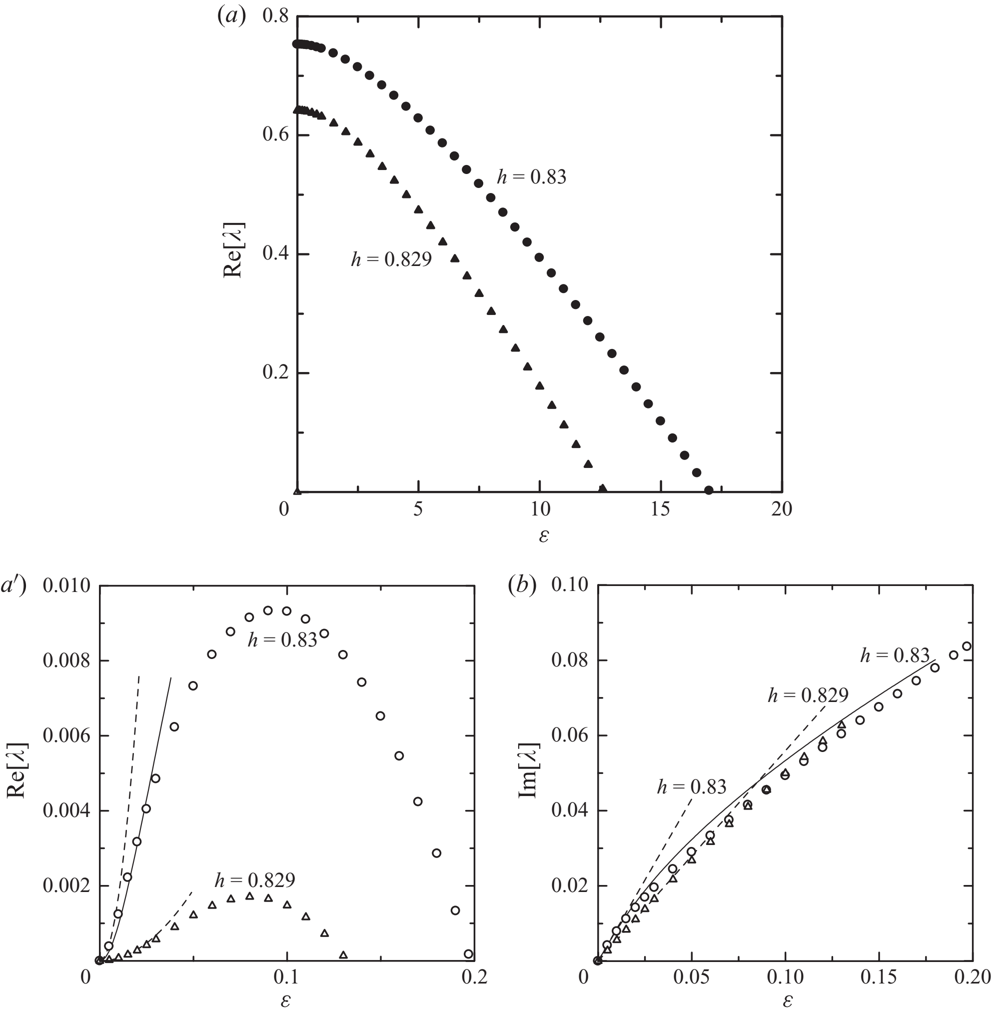

FIGURE 11. Computed eigenvalues λ with a positive real part versus ε for $h = 0.829$ (▲, △) and 0.83 (●, ○), where the black and white markers represent numerical results for the real and complex eigenvalues, respectively: (*a*) Re[λ] versus ε; (*a*′) enlarged view of (*a*) near the origin; (*b*) Im[λ] versus ε. See caption of figure 4 for the dashed line. The solid line for $h = 0.83$ is the asymptotic solution (A 25*b*) that takes into account the effect of small $|\mathrm{d}E/\mathrm{d}v|$.

4.3. *Solitary waves longitudinally unstable to two modes* ($0.83028 < h < 0.83305$)

We computed at least every 0.02, 0.5 and 2 in ε in the ranges of $\varepsilon \leqslant 1$, $1 < \varepsilon \leqslant 20$ and $20 < \varepsilon \leqslant 300$, respectively. The λ versus ε profiles for $h = 0.8309$, 0.83097, 0.830976, 0.830977 and 0.831 thus obtained are plotted in figure 12. The dashed lines are the ordinary asymptotic solution (2.16) for small ε, whereas the solid lines for $h = 0.830976$ and 0.830977 are the solution (B 25) that takes into account the effect of small $|\mathrm{d}v/\mathrm{d}h|$ ($\mathrm{d}v/\mathrm{d}h = 0$ at $h = 0.8309762$; see figure 1*b*). These asymptotic solutions agree well with the corresponding numerical results for small ε and $|\lambda|$.

We find from figure 12(*a*′) for $h = 0.8309$ that λ versus ε for $h = 0.8309$ is similar to those for $h = 0.785$, 0.79 and 0.795 (see figure 7*a*) in the sense that two different real branches starting from $\varepsilon = 0$ merge at some wavenumber $\varepsilon = \varepsilon_{merge}$, becoming

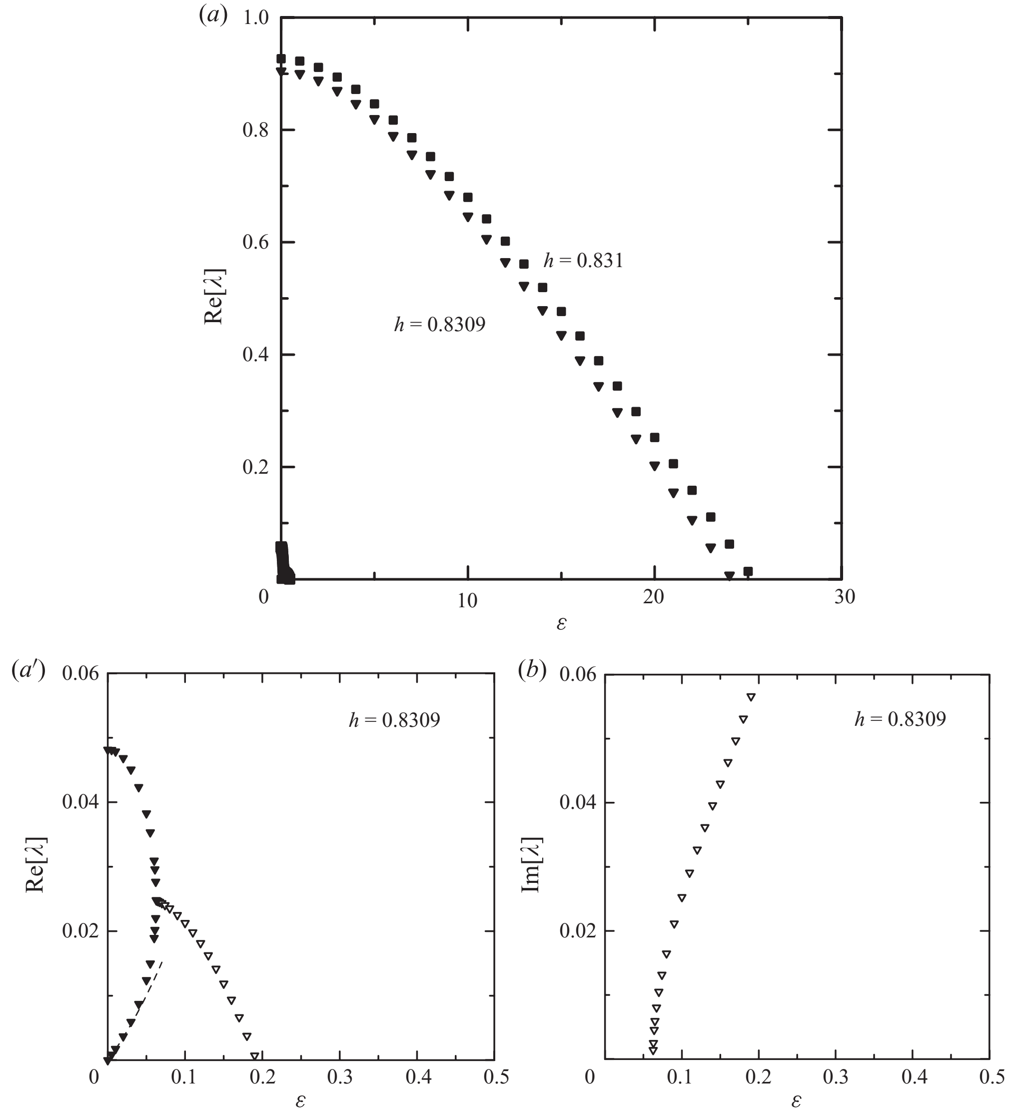

FIGURE 12. For caption see page 148.

a single complex branch running from $\varepsilon = \varepsilon_{merge}$ to ε_C. The difference is that there is an additional real branch (the first real branch) of large positive eigenvalues for $h = 0.8309$, as shown in figure 12(*a*). Table 4 arranges the cutoff wavenumbers ε_C and ε_{R1} of the complex and the first real branches together with the merging wavenumber ε_{merge}. Figure 12(*a*′) for $h = 0.83097$ shows that an arc-shaped branch of real eigenvalues appears from the axis $\mathrm{Re}[\lambda] = 0$ with both ends placed on the axis $\mathrm{Re}[\lambda] = 0$. The end points, denoted by $\varepsilon = \varepsilon_S$ and ε_L, are tabulated in table 4. As in the case of solitary waves unstable to a single longitudinal mode, this arc-shaped branch approaches the pre-existing real branch and partly merges with it, forming a single complex branch (see figure 12(*a*′, *a*″) for $h = 0.830976$). This complex branch extends its range to the origin and the larger-ε side, and finally reaches the origin at $h = 0.8309762$ (see figure 12*a*′ for $h = 0.830977$) and the pre-existing complex branch

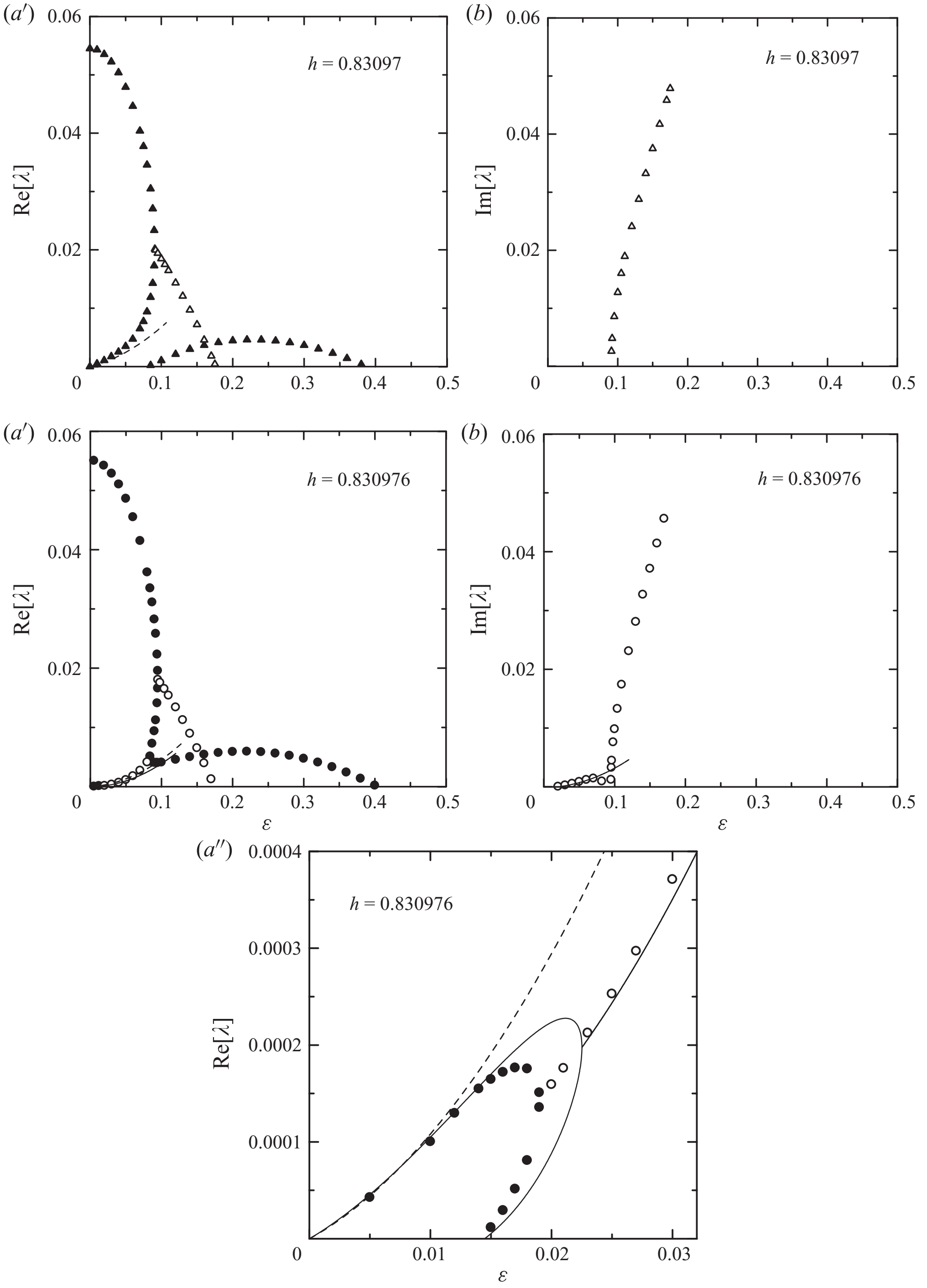

FIGURE 12. For caption see page 148.

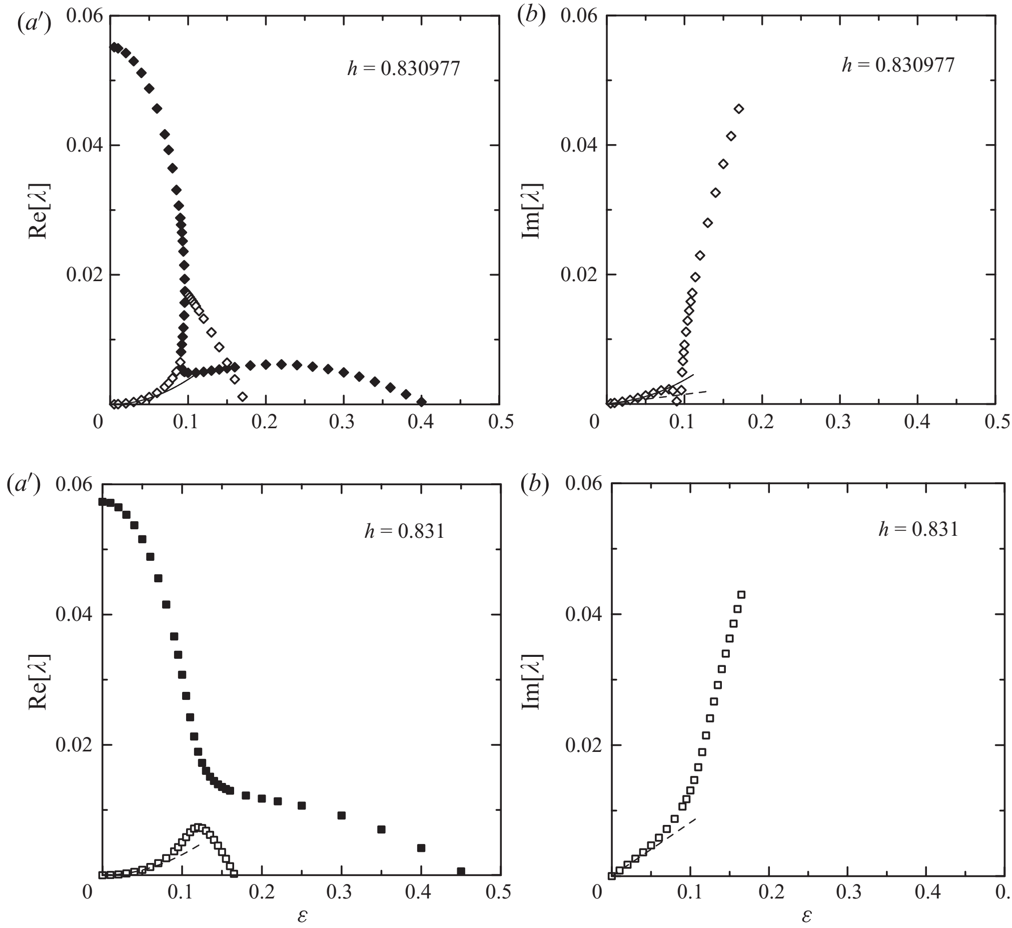

FIGURE 12. Computed eigenvalues λ with a positive real part versus ε for $h=0.8309$ (▼, ▽), 0.83097 (▲, △), 0.830976 (●, ○), 0.830977 (◆, ◇) and 0.831 (■, □), where the black and white markers represent numerical results for the real and complex eigenvalues, respectively: (*a*) $\mathrm{Re}[\lambda]$ versus ε ($h=0.8309$ and 0.831); (*a*′) enlarged view of (*a*) near the origin; (*a*″) further enlarged view of (*a*′) for $h=0.830976$ near the origin; (*b*) $\mathrm{Im}[\lambda]$ versus ε. See caption of figure 4 for the dashed line. The solid line for h =0.830976 and 0.830977 is the asymptotic solution (B 25) that takes into account the effect of small $|\mathrm{d}v/\mathrm{d}h|$. Note that the dashed line in (*a*′) for $h=0.830977$ is superposed on the solid line. The results for $h=0.83097$, 0.830976 and 0.830977 are not shown in (*a*), since they nearly overlap the results for $h=0.8309$ and 0.831.

on the larger-ε side at $h=0.830980$. Finally, there exist three independent unstable branches: two newly generated branches, namely the complex one and the real one (the latter is called the second real branch), and the pre-existing first real branch, as shown in figure 12(*a*, *a*′) for $h=0.831$. Their cutoff wavenumbers ε_C (complex), ε_{R1} (first real) and ε_{R2} (second real) are tabulated in table 4.

The above complex branch approaches the axis $\mathrm{Re}[\lambda]=0$ as h increases, and finally disappears into the axis $\mathrm{Re}[\lambda]=0$ at $h=0.83108$ when Q changes sign to positive (see figure 1*b*). Figure 13 for $h=0.832$ is an example of λ versus ε after such disappearance. There is no complex branch; only the first and second real branches exist. Their cutoff wavenumbers ε_{R1} and ε_{R2} are tabulated in table 4. At $h=0.83292$, Q becomes negative

h	ε_{merge}	ε_S	ε_L	ε_C	ε_{R1}	ε_{R2}	Class of instability
0.8309	0.063	–	–	0.192	24	–	R_0
0.83097	0.091	0.081	0.39	0.176	25	–	R_1
0.830976	0.095	0.014	0.40	0.175	25	–	R_2
0.830977	–	–	–	0.174	25	0.41	C_1
0.831	–	–	–	0.166	25	0.46	C_0
0.832	–	–	–	–	47	1.9	N
0.833	–	–	–	0.166	276	14	C_0

TABLE 4. Merging wavenumber ε_{merge} of two real branches starting from $\varepsilon = 0$, smaller- and larger-end wavenumbers ε_S and ε_L of arc-shaped real branch, and cutoff wavenumbers ε_C, ε_{R1} and ε_{R2} of complex, the first real and the second real branches of eigenvalues, respectively, when the solitary wave is unstable to two longitudinal disturbance modes ($0.83028 < h < 0.83305$). See §4.4 for the class of instability and figure 15 for typical profiles of Re[λ] versus ε.

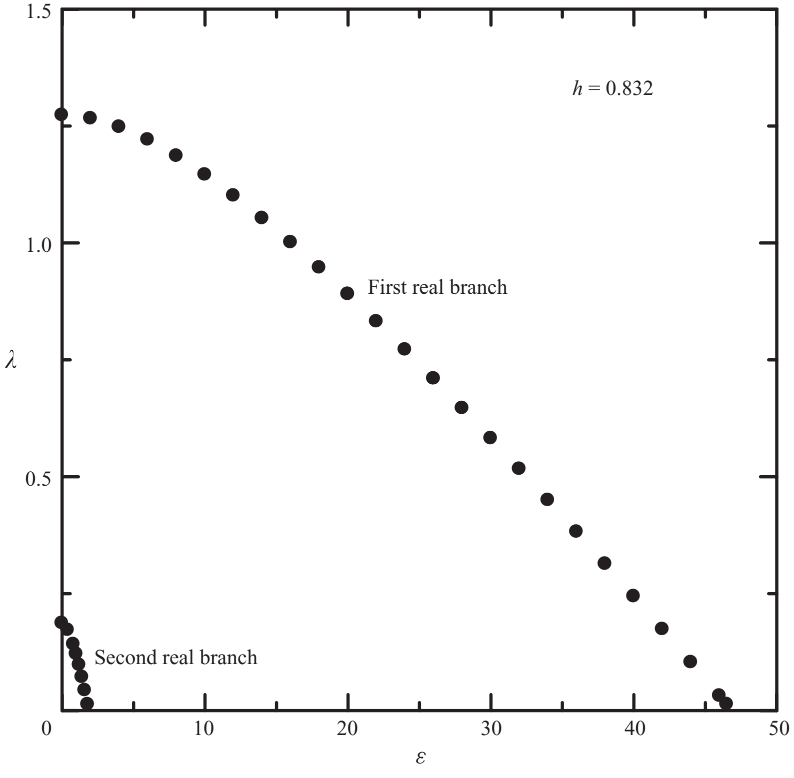

FIGURE 13. Computed eigenvalues λ with a positive real part (which are all real) versus ε for $h = 0.832$.

again (see figure 1c), and the complex branch reappears. Figure 14 for $h = 0.833$ is an example of λ versus ε after such reappearance, and figure 14(a') clearly shows the existence of the unstable complex branch. The corresponding cutoff wavenumber ε_C, together with those of the first and second real branches, ε_{R1} and ε_{R2}, are tabulated in table 4.

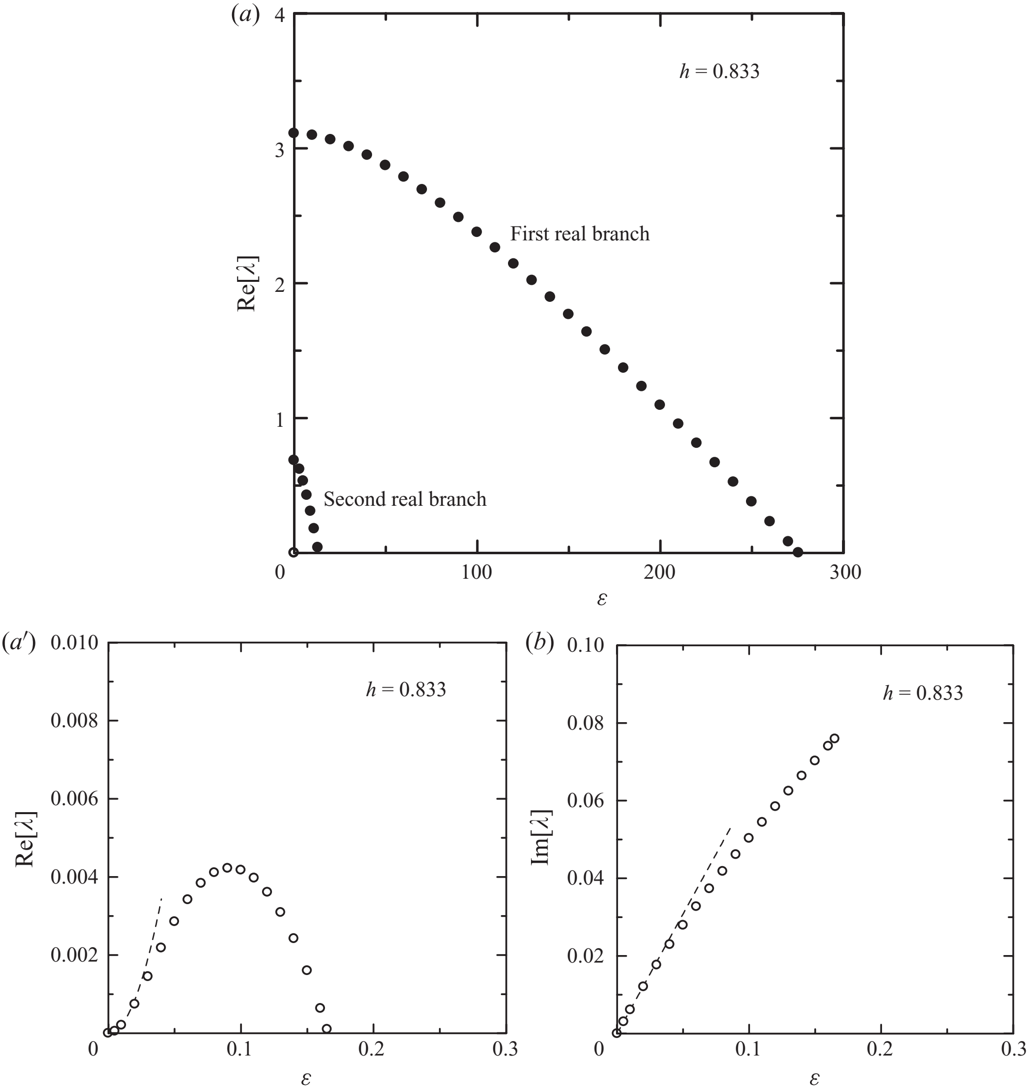

FIGURE 14. Computed eigenvalues λ with a positive real part versus ε for $h = 0.833$: (a) Re[λ] versus ε; (a') enlarged view of (a) near the origin; (b) Im[λ] versus ε. ● and ○ denote numerical results for the real and complex eigenvalues, respectively. See caption of figure 4 for the dashed line.

4.4. *Classification of transverse instability*

There is a similarity in the profiles of λ versus ε. For instance, similarity is found between those for $h = 0.82$ and 0.832 (which we will call Class N); those for $h = 0.797$ and 0.831 (Class C_0); those for $h = 0.79595$ and 0.830977 (Class C_1); those for $h = 0.79$ and 0.8309 (Class R_0); those for $h = 0.7958$ and 0.83097 (Class R_1); and those for $h = 0.7959$ and 0.830976 (Class R_2). The only difference in each pair is that there is an additional real branch of large positive eigenvalues for the latter case because the solitary wave in the former case is unstable to a single longitudinal mode, whereas the solitary wave in the latter case is unstable to two modes. Typical profiles of Re[λ] versus ε are illustrated in figure 15, where m is the number of growing longitudinal

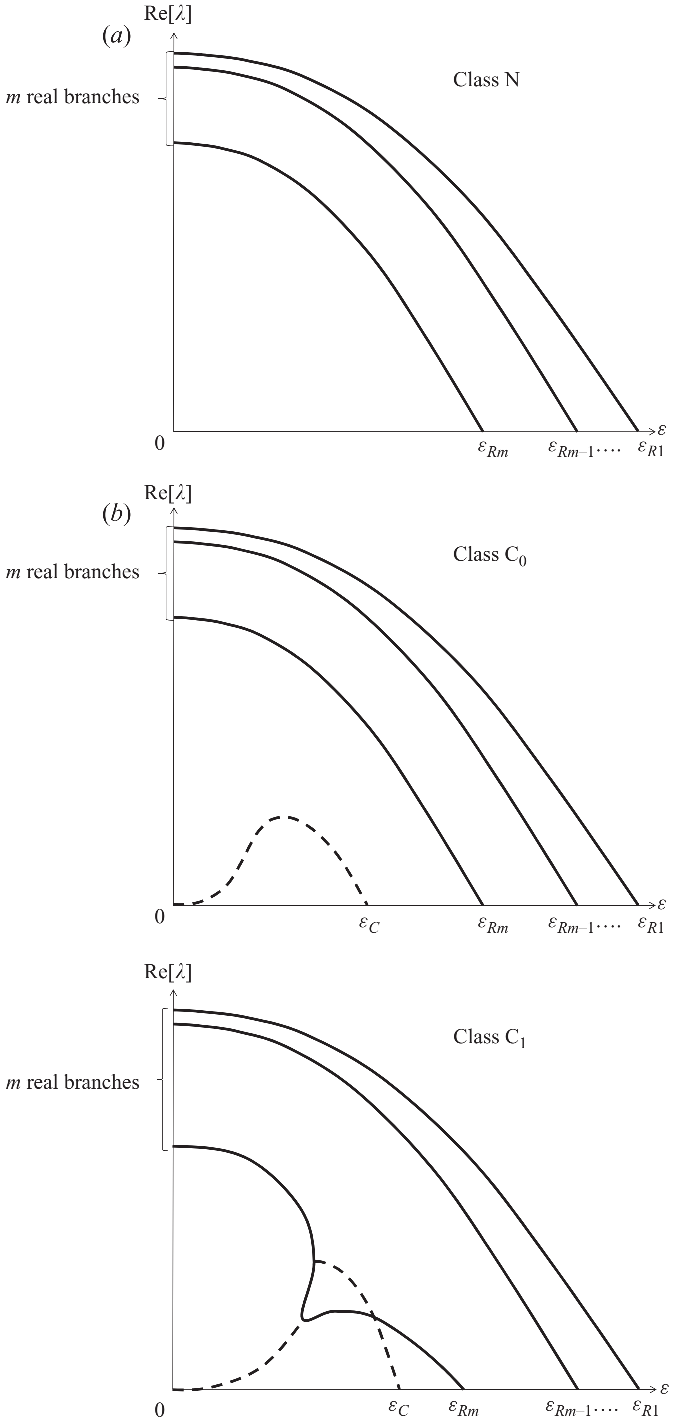

FIGURE 15. For caption see next page.

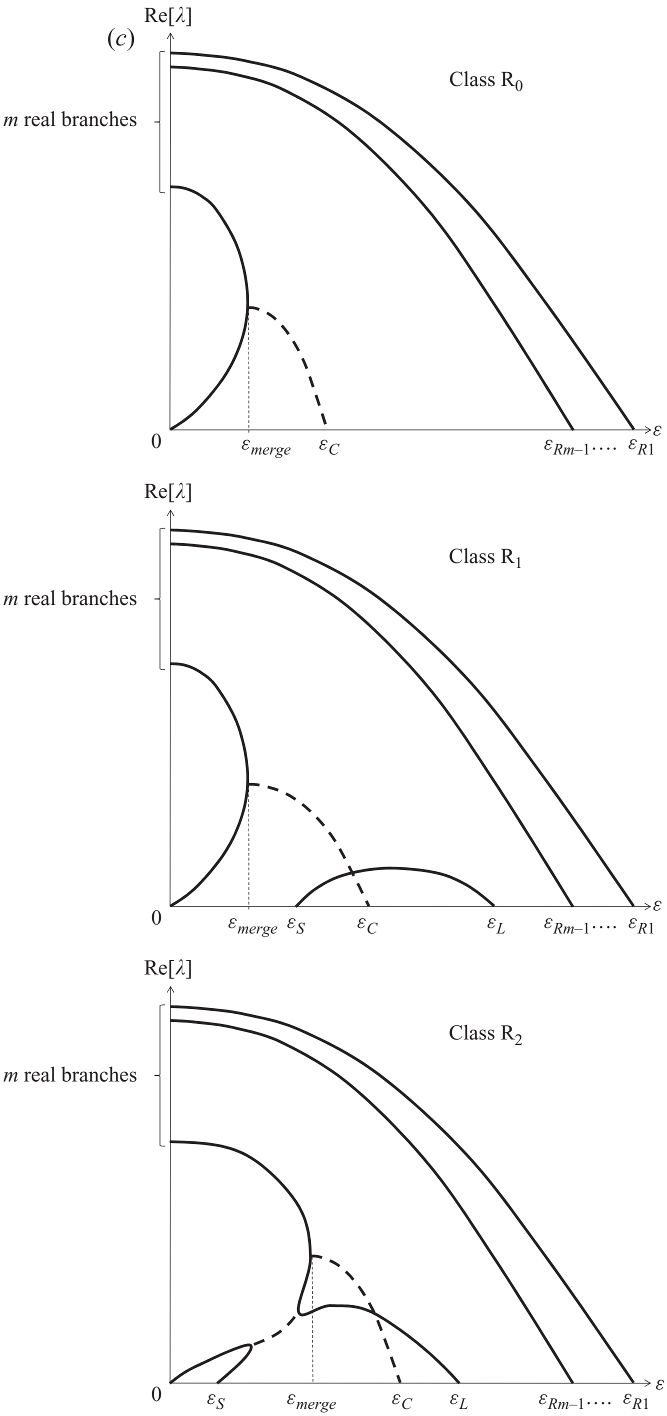

FIGURE 15. Typical profiles of $\mathrm{Re}[\lambda]$ versus ε: (*a*) Class N ($\mathrm{d}E/\mathrm{d}v > 0$ and $Q > 0$); (*b*) Classes C_0 and C_1 ($\mathrm{d}E/\mathrm{d}v > 0$ and $Q < 0$); (*c*) Classes R_0, R_1 and R_2 ($\mathrm{d}E/\mathrm{d}v < 0$). The solid and dashed lines represent the real and complex solution branches, respectively, and m is the number of growing longitudinal disturbance modes having $\mathrm{Re}[\lambda] > 0$ at $\varepsilon = 0$.

disturbance modes having $\mathrm{Re}[\lambda] > 0$ at $\varepsilon = 0$. The classification of transverse instability (into three basic classes N, C and R, and further into six subclasses N, C_0, C_1, R_0, R_1 and R_2) is as follows.

(i) Class N: no unstable branch is connected to the origin on the $\varepsilon - \mathrm{Re}[\lambda]$ plane. A typical profile of $\mathrm{Re}[\lambda]$ versus ε is illustrated in figure 15(*a*). This basic class appears for $\mathrm{d}E/\mathrm{d}v > 0$ and $Q > 0$.

(ii) Class C: an unstable branch of complex eigenvalues is connected to the origin on the $\varepsilon - \mathrm{Re}[\lambda]$ plane. More precisely, if the other end of the above complex branch is located on the axis $\mathrm{Re}[\lambda] = 0$, we call it Class C_0, and if the above complex branch is interrupted by a real branch on its way, we call it Class C_1. Typical profiles of $\mathrm{Re}[\lambda]$ versus ε are illustrated in figure 15(*b*). This basic class C appears for $\mathrm{d}E/\mathrm{d}v > 0$ and $Q < 0$, in which Class C_1 occurs only in a limited range of h near the amplitude for $\mathrm{d}v/\mathrm{d}h = 0$.

(iii) Class R: an unstable branch of real eigenvalues is connected to the origin on the $\varepsilon - \mathrm{Re}[\lambda]$ plane. More precisely, if the other end of the above real branch is located on the axis $\varepsilon = 0$, we call it Class R_1 or R_0 depending on whether there is an arc-shaped branch of real eigenvalues (whose two ends are placed on the axis $\mathrm{Re}[\lambda] = 0$). If the above real branch is interrupted on its way to the axis $\varepsilon = 0$ by a complex branch, we call it Class R_2. Typical profiles of $\mathrm{Re}[\lambda]$ versus ε are illustrated in figure 15(*c*). This basic class R appears for $\mathrm{d}E/\mathrm{d}v < 0$, in which Classes R_1 and R_2 occur only in a limited range of h near the amplitude for $\mathrm{d}v/\mathrm{d}h = 0$.

For instance, the transverse instability for $h = 0.797$ is called 'Class C_0 with $m = 1$', since there is an unstable complex branch that is connected to the origin and the axis $\mathrm{Re}[\lambda] = 0$ (Class C_0), and the solitary wave is unstable to a single longitudinal disturbance mode ($m = 1$).

Let us see how the class of transverse instability changes as h increases from small amplitude $h \ll 1$. For $h < 0.7133$ there is no eigenvalue with a positive real part, and this type is called Class N with $m = 0$. For $0.7133 < h < 0.7807$, there is an unstable complex branch which is connected to the origin and the axis $\mathrm{Re}[\lambda] = 0$ (see figures 4 and 5*a*). This type is called Class C_0 with $m = 0$.

For larger h between 0.7807 and 0.83028, the solitary wave is unstable to a single longitudinal mode ($m = 1$). The following classes appear in increasing order of h:

$$\text{Class R}\left\{\begin{array}{lll} {\scriptstyle 0} & \text{for} & 0.7807 < h < 0.7951 \\ {\scriptstyle 1} & \text{for} & 0.7951 < h < 0.79587 \\ {\scriptstyle 2} & \text{for} & 0.79587 < h < 0.79591 \end{array}\right\} : \mathrm{d}E/\mathrm{d}v < 0,$$

$$\text{Class C}\left\{\begin{array}{lll} {\scriptstyle 1} & \text{for} & 0.79591 < h < 0.795955 \\ {\scriptstyle 0} & \text{for} & 0.795955 < h < 0.79803 \end{array}\right\} : \mathrm{d}E/\mathrm{d}v > 0 \quad \text{and} \quad Q < 0,$$

$$\text{Class N} \quad \text{for} \quad 0.79803 < h < 0.82811 \; : \mathrm{d}E/\mathrm{d}v > 0 \quad \text{and} \quad Q > 0,$$

$$\text{Class C}_0 \quad \text{for} \quad 0.82811 < h < 0.83028 \; : \mathrm{d}E/\mathrm{d}v > 0 \quad \text{and} \quad Q < 0.$$

Note that the marginal classes of instability, i.e. Classes C_1, R_1 and R_2, occur only in a limited range of h near the amplitude $h = 0.79591$ for $\mathrm{d}v/\mathrm{d}h = 0$ (see figure 1*a*).

For larger h between 0.83028 and 0.83305, the solitary wave is unstable to two longitudinal modes ($m = 2$), and the results in § 4.3 indicate that the same classes of transverse instability occur as those for $m = 1$. Thus, the classes of transverse

h	$2x(\eta_s=0.5h)$	$2x(\eta_s=0.9h)$	$2x(\eta_s=0.99h)$
0.76	2.112	0.584	0.163
0.78	2.023	0.527	0.143
0.796	1.946	0.471	0.123
0.83	1.789	0.307	0.042
0.831	1.787	0.303	0.038
0.833	1.782	0.297	0.030

TABLE 5. Horizontal widths $2x$ of the unperturbed solitary waves at $\eta_s=0.5h$, $0.9h$ and $0.99h$.

instability that occur in increasing order of h from small amplitude $h \ll 1$ are

$$\left.\begin{array}{l} \mathrm{N} \rightarrow \mathrm{C}_0 \quad \text{for} \quad m=0, \\ \rightarrow \mathrm{R}\{_0{\rightarrow}_1{\rightarrow}_2\} \rightarrow \mathrm{C}\{_1{\rightarrow}_0\} \rightarrow \mathrm{N} \rightarrow \mathrm{C}_0 \quad \text{for} \quad m=1, \\ \rightarrow \mathrm{R}\{_0{\rightarrow}_1{\rightarrow}_2\} \rightarrow \mathrm{C}\{_1{\rightarrow}_0\} \rightarrow \mathrm{N} \rightarrow \mathrm{C}_0 \quad \text{for} \quad m=2, \\ \rightarrow \ldots . \end{array}\right\} \tag{4.1}$$

It is expected that a repetition of the same cycle, $\rightarrow \mathrm{R}\{_0{\rightarrow}_1{\rightarrow}_2\} \rightarrow \mathrm{C}\{_1{\rightarrow}_0\} \rightarrow \mathrm{N} \rightarrow \mathrm{C}_0$, continues for $m \geqslant 3$, although this speculation has not been confirmed numerically.

It is convenient to use figure 1 in order to find the corresponding basic class of transverse instability when the amplitude h of the solitary wave is given. In fact, Class N appears on the dotted line, Class C on the thin solid line and Class R on the thick solid line, because $\mathrm{d}E/\mathrm{d}v>0$ and $Q>0$ on the dotted line, $\mathrm{d}E/\mathrm{d}v>0$ and $Q<0$ on the thin solid line, and $\mathrm{d}E/\mathrm{d}v<0$ on the thick solid line. The number m can be determined by the number of times the curve passes through the crosses when the solution branch is traced from small amplitude $h \ll 1$. In this way, we can easily obtain the corresponding basic class of transverse instability for given h from figure 1.

Finally in this section, we should note that there is a high-wavenumber cutoff to all the transverse instability investigated here. Any transversely unstable solitary waves become stable to a disturbance of transverse wavenumber higher than some critical value ε_{cri} which depends on the wave amplitude h (e.g. $\varepsilon_{cri}=0.205$, 1.5 and 17 for $h=0.78$, 0.81 and 0.83, respectively). We have confirmed this fact up to $h \leqslant 0.833$, which is very near the limiting value 0.83322.

5. Eigenfunctions (surface profiles of growing disturbance modes)

Numerical results on eigenfunctions (surface profiles of growing disturbance modes) are presented here. For the sake of comparison, horizontal widths $2x$ of the unperturbed solitary waves at $\eta_s=0.5h$, $0.9h$ and $0.99h$ are tabulated in table 5. Results on eigenfunctions are given in separate subsections for three different types of solitary waves: longitudinally stable ones in § 5.1, those longitudinally unstable to a single mode in § 5.2, and those longitudinally unstable to two modes in § 5.3.

5.1. *Longitudinally stable solitary waves* ($h<0.7807$)

The surface profile $\hat{\eta}$ of a growing disturbance mode is shown in figure 16 ($h=0.76$) and figure 17 ($h=0.78$). The surface profile $\hat{\eta}$ is complex and arbitrary under multiplication by a complex constant. Such arbitrariness is removed here by imposing the following normalization:

$$\max|\mathrm{Re}\,[\hat{\eta}]|=1, \qquad \int_{-\infty}^{\infty} \mathrm{Im}\,[\hat{\eta}]\,\frac{\mathrm{d}\eta_s}{\mathrm{d}x}\,\mathrm{d}x=0, \tag{5.1a,b}$$

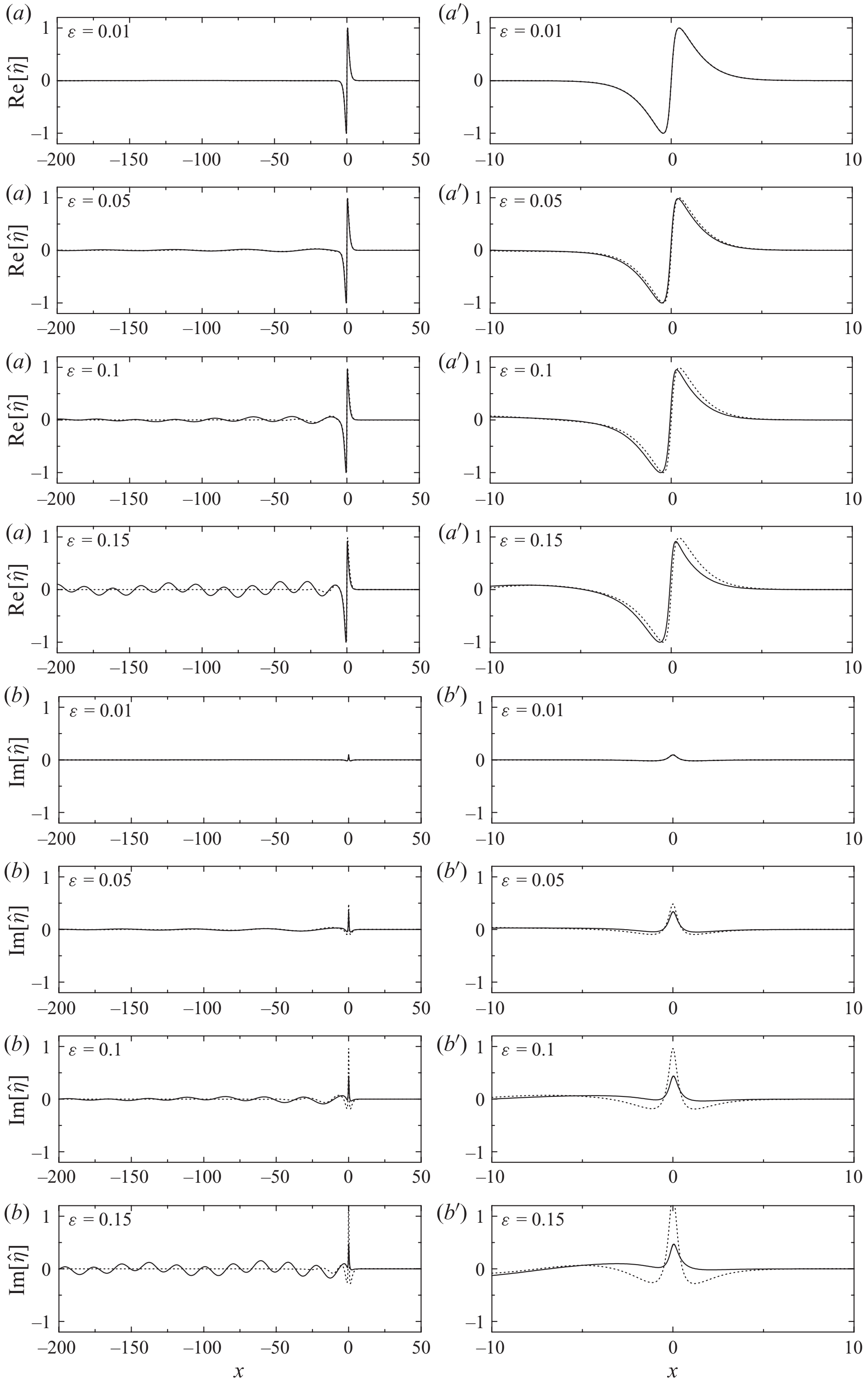

FIGURE 16. For caption see next page.

where the first one normalizes the profile $\hat{\eta}$ by the maximum value of $|\mathrm{Re}[\hat{\eta}]|$. The sign of $\hat{\eta}$ is chosen such that

$$\int_{-\infty}^{\infty} \mathrm{Re}\,[\hat{\eta}]\,\frac{\mathrm{d}\eta_s}{\mathrm{d}x}\,\mathrm{d}x < 0. \tag{5.1c}$$

The solid lines in figures 16 and 17 are numerical results thus obtained. The dotted lines are the asymptotic solution for small ε given by (3.1), (3.9) and (3.22) of Kataoka & Tsutahara (2004*a*) under the above normalization (5.1), and the dash-dot lines plotted only for $h = 0.78$ in figure 17 are the asymptotic solution (A 2), (A 11*b*) and (A 19) that takes into account the effect of small $|\mathrm{d}E/\mathrm{d}v|$ ($\mathrm{d}E/\mathrm{d}v = 0$ at $h = 0.7807$). When $h = 0.76$, the former (dotted line) agrees well with the numerical result (solid line) for small ε (up to around $\varepsilon \leqslant 0.05$), and when $h = 0.78$, the latter (dash-dot line) agrees well with the numerical result for small ε (up to around $\varepsilon \leqslant 0.03$). Thus, the surface profile of a growing disturbance mode for small ε can be represented by either of the asymptotic solutions. For larger ε, however, these asymptotic solutions do not agree well with the numerical results, as shown in figures 16 and 17.

In the far field behind the core of the solitary wave, a physical interpretation of the wave motion can be given as follows. In this region, linear waves of transverse wavenumber ε propagate. They are radiated from the core of the solitary wave by harmonic resonance with oscillations of a distorted solitary wave whose angular frequency is $\mathrm{Im}[\lambda]$ and whose amplitude grows like $\exp(\mathrm{Re}[\lambda]t)$. The x- and t-dependence of radiated waves is expressed as $\exp(k_n x + \lambda t)$ ($n = 1, 2, \ldots$), where k_n are solutions of the linear dispersion relationship:

$$\lambda = k_n v \pm \mathrm{i}\sqrt{\sqrt{-k_n^2 + \varepsilon^2}\tanh\sqrt{-k_n^2 + \varepsilon^2}}, \tag{5.2}$$

with λ being substituted from the numerical result. There are many solutions k_n for a given λ. In the present case where λ is complex, all these solutions k_n become complex. Especially when the real part $\mathrm{Re}[\lambda]$ of complex eigenvalue λ is positive and small, which holds true for the present case, two solutions k_n (say k_1 and k_2) have positive real parts that are much smaller than the other solutions of k_n. For instance, $(\mathrm{Re}[k_1], \mathrm{Re}[k_2]) = (0.003, 0.008)$, $(0.005, 0.011)$ and $(0.002, 0.003)$ for $\varepsilon = 0.05$, 0.1 and 0.15, respectively, when $h = 0.76$, and $(0.008, 0.024)$, $(0.015, 0.031)$ and $(0.011, 0.020)$ for $\varepsilon = 0.03$, 0.1 and 0.15, respectively, when $h = 0.78$. These waves of the two smallest decaying rates $\mathrm{Re}[k_1]$ and $\mathrm{Re}[k_2]$ decay slowly as $x \to -\infty$ so that they remain non-zero even far behind the solitary wave. Their wavenumbers $|\mathrm{Im}[k_1]|$ and $|\mathrm{Im}[k_2]|$ are larger for larger ε. Specifically, $(\mathrm{Im}[k_1], \mathrm{Im}[k_2]) = (0.020, 0.13)$, $(0.046, 0.23)$ and $(0.076, 0.33)$ for $\varepsilon = 0.05$, 0.1 and 0.15, respectively, when $h = 0.76$, and $(0.008, 0.08)$, $(0.049, 0.22)$ and $(0.081, 0.31)$ for $\varepsilon = 0.03$, 0.1 and 0.15, respectively, when $h = 0.78$. These results on the x-dependence of radiated waves obtained from the linear dispersion relationship (5.2) agree well with those observed in surface profiles $\hat{\eta}$ for $x < 0$ presented in figures 16(*a*, *b*) and 17(*a*, *b*) especially for $\varepsilon \geqslant 0.1$. For

---

FIGURE 16. Surface profile $\hat{\eta}$ of a growing disturbance mode for $h = 0.76$ ($\varepsilon = 0.01$, 0.05, 0.1, 0.15): (*a*) $\mathrm{Re}[\hat{\eta}]$ versus x; (*a*′) enlarged view of (*a*) in the core region ($-10 < x < 10$); (*b*) $\mathrm{Im}[\hat{\eta}]$ versus x; (*b*′) enlarged view of (*b*) in the core region ($-10 < x < 10$). The solid line is the numerical result, and the dotted line is the asymptotic solution for small ε given by (3.1), (3.9) and (3.22) of Kataoka & Tsutahara (2004*a*). Both profiles are normalized by (5.1). The dotted line is almost superposed on the solid line for $\varepsilon = 0.01$.

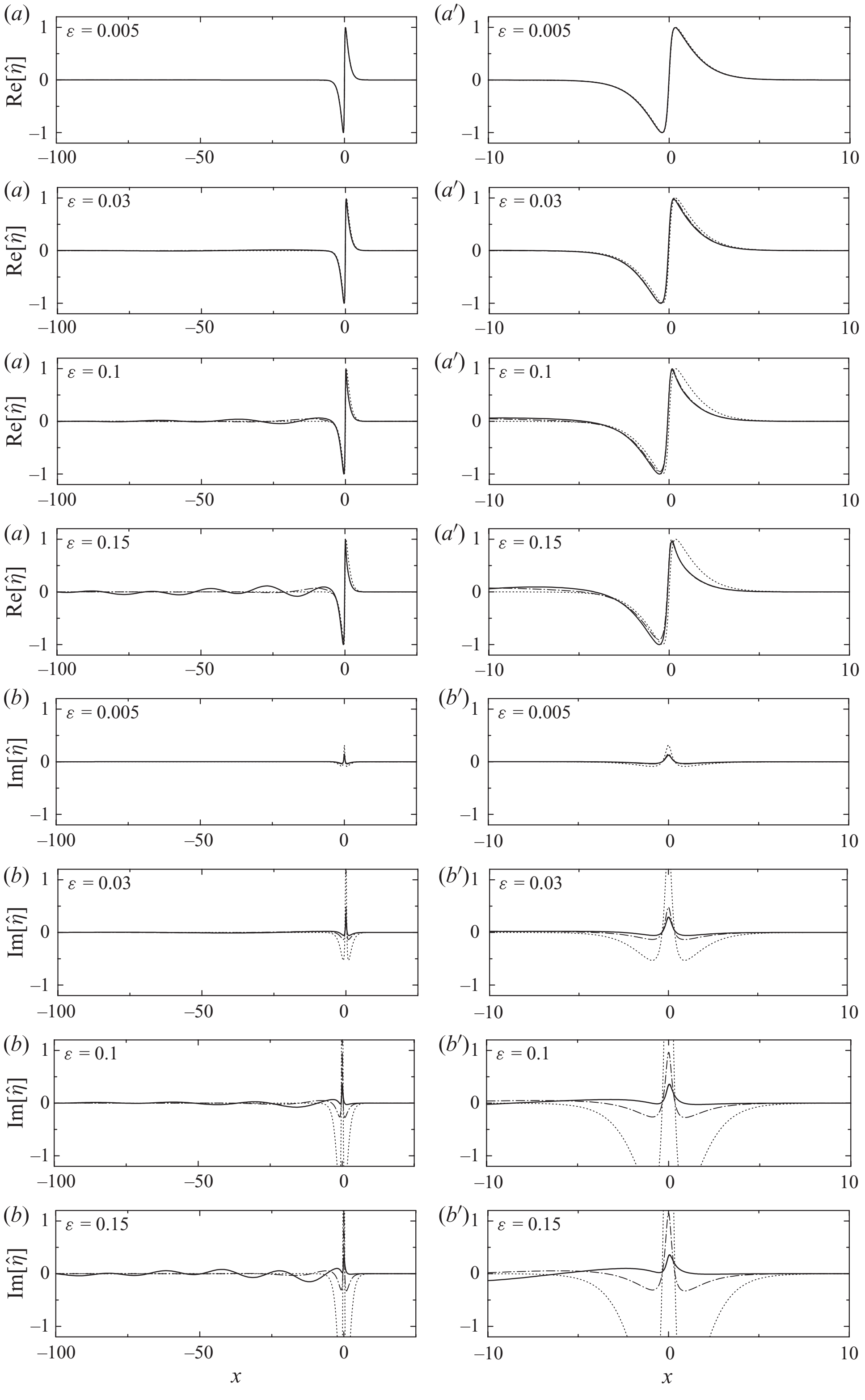

FIGURE 17. For caption see next page.

smaller ε, it is difficult to discern radiated waves because their amplitudes become much smaller as ε decreases.

5.2. *Solitary waves longitudinally unstable to a single mode* ($0.7807 < h < 0.83028$)

The qualitative features of $\hat{\eta}$ when the corresponding eigenvalue is complex are basically the same as those presented in § 5.1. Here we discuss the case where the corresponding eigenvalue is real. Figure 18 shows the surface profiles $\hat{\eta}$ (which are real) of growing disturbance modes for $h = 0.796$ and 0.83 whose eigenvalues are on the first real branch. The normalization (5.1*a*,*c*) is applied. The profiles $\hat{\eta}$ in the core region have a forward peak and a rather gradual tail depression. Their horizontal length scale in the core region diminishes considerably as h increases (see figure 18*a*′ for $h = 0.796$ and figure 18*b*′ for $h = 0.83$), whereas it is almost unchanged with respect to the variation of ε.

In the far field behind the core of the solitary wave, evanescent waves appear in the present case where λ is real. Their x- and t-dependence is expressed as $\exp(k_n x + \lambda t)$ ($n = 1, 2, \ldots$), where k_n are solutions of the linear dispersion relationship (5.2) for a positive real λ. In fact, k_n are all real or two of them become a complex-conjugate pair having a positive real part. In general, a complex-conjugate pair appears unless both ε and λ are small (e.g. it appears for $\varepsilon \geqslant 0.058$ when $h = 0.796$ and for $\varepsilon \geqslant 0$ when $h = 0.83$). When k_n are all real, the surface profile $\hat{\eta}$ behind the solitary wave decays monotonically as $x \to -\infty$. When k_n include a pair of complex conjugates of the form $k_r \pm \mathrm{i}k_\mathrm{i}$ ($k_r, k_i > 0$), which occur in general, the surface profile behind the solitary wave looks oscillatory in x because the evanescent waves corresponding to complex $k_n = k_r \pm \mathrm{i}k_i$ propagate not along the x-coordinate but along $\pm k_i x + \varepsilon y = \text{constant}$ diagonally. Here k_r and k_i represent, respectively, the decay rate and the wavenumber in x of diagonally radiated evanescent waves. Specifically, $(k_r, k_i) = (0.033, 0.12)$, $(0.015, 0.23)$ and $(0.006, 0.43)$ for $\varepsilon = 0.1$, 0.2 and 0.4, respectively, when $h = 0.796$, and $(0.52, 1.8)$, $(0.31, 2.5)$ and $(0.094, 3.0)$ for $\varepsilon = 5$, 10 and 15, respectively, when $h = 0.83$. These results for k_r and k_i obtained from the linear dispersion relationship (5.2) agree with those observed in surface profiles $\hat{\eta}$ for $x < 0$ presented in figure 18(*a*, *b*) especially for $\varepsilon \geqslant 0.2$ ($h = 0.796$) and $\varepsilon \geqslant 10$ ($h = 0.83$). For smaller ε, it is difficult to discern evanescent waves because their amplitudes become much smaller as ε decreases.

5.3. *Solitary waves longitudinally unstable to two modes* ($0.83028 < h < 0.83305$)

Figure 19 shows the surface profiles $\hat{\eta}$ of growing disturbance modes for $h = 0.831$ and 0.833 whose eigenvalues are on the second real branch (see figures 12*a*′ and 14*a*). The profiles $\hat{\eta}$ in the core region have a sharp-pointed depression at $x = 0$, together with a rather gradual forward elevation (for $x > 0$) and a tail depression (for $x < 0$). Their horizontal length scale in the core region diminishes considerably as h increases (see figure 19*a*′ for $h = 0.831$ and figure 19*b*′ for $h = 0.833$), whereas it is almost unchanged with respect to the variation of ε. As for the profile $\hat{\eta}$ behind the solitary wave, evanescent waves appear in accordance with λ being real, as in § 5.2. The decay rate k_r and the wavenumber k_i in x of diagonally radiated evanescent waves calculated

---

FIGURE 17. Surface profile $\hat{\eta}$ of a growing disturbance mode for $h = 0.78$ ($\varepsilon = 0.005$, 0.03, 0.1, 0.15): (*a*) $\mathrm{Re}[\hat{\eta}]$ versus x; (*a*′) enlarged view of (*a*) in the core region ($-10 < x < 10$); (*b*) $\mathrm{Im}[\hat{\eta}]$ versus x; (*b*′) enlarged view of (*b*) in the core region ($-10 < x < 10$). See caption of figure 16 for the solid and dotted lines. The dash-dot line represents the asymptotic solution (A 2), (A 11*b*) and (A 20) that takes into account the effect of small $|\mathrm{d}E/\mathrm{d}v|$ and is normalized by (5.1). The dash-dot line is almost superposed on the solid line for $\varepsilon = 0.005$ and 0.03.

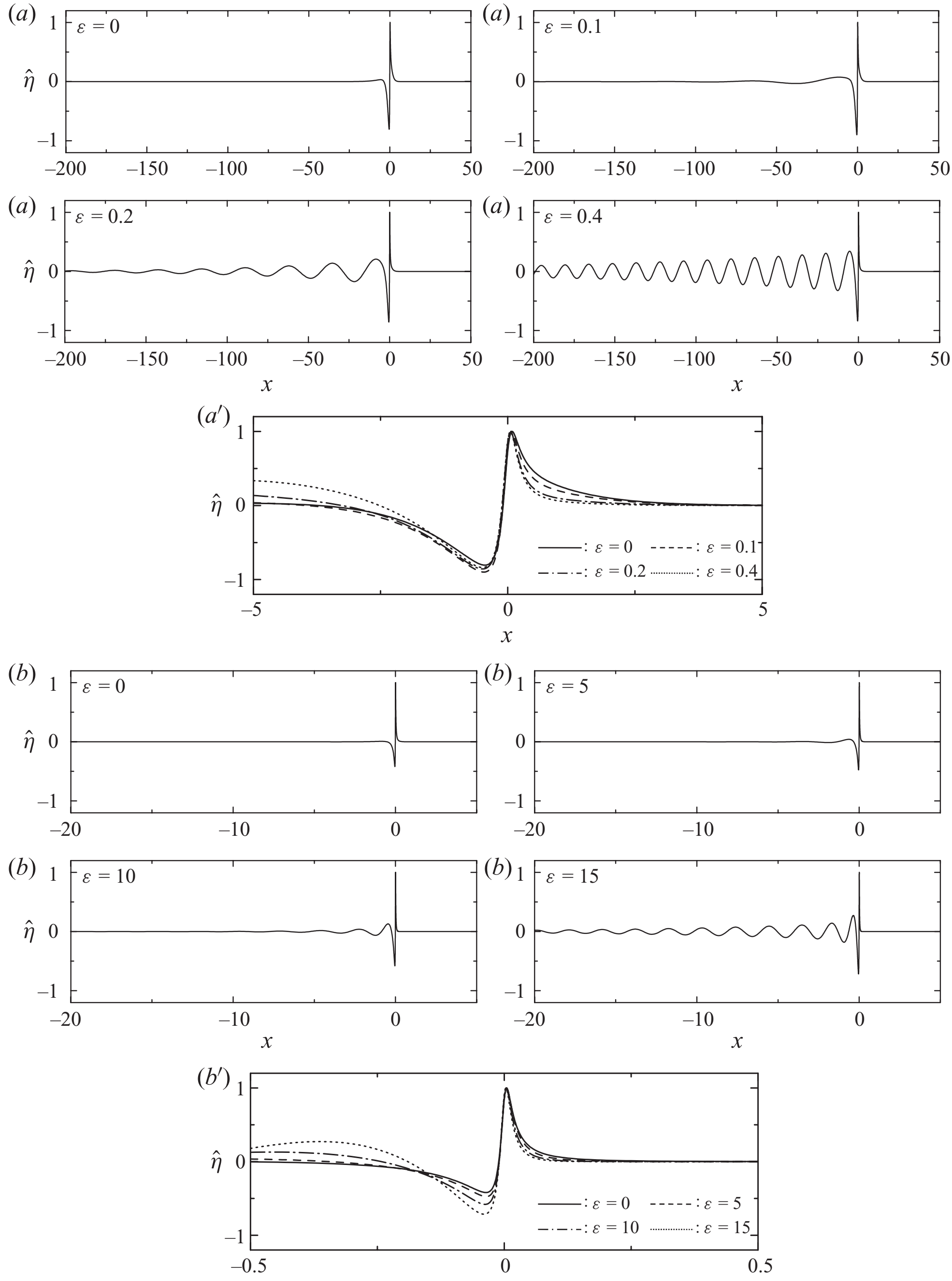

FIGURE 18. Surface profile $\hat{\eta}$ of a growing disturbance mode whose eigenvalue is on the first real branch: (*a*) $h = 0.796$ ($\varepsilon = 0$, 0.1, 0.2, 0.4); (*a*′) enlarged view of (*a*) in the core region ($-5 < x < 5$); (*b*) $h = 0.83$ ($\varepsilon = 0$, 5, 10, 15); (*b*′) enlarged view of (*b*) in the core region ($-0.5 < x < 0.5$). All profiles are numerical results normalized by (5.1), and the result for $\varepsilon = 0$ is obtained by the numerical method in Kataoka (2006*a*).

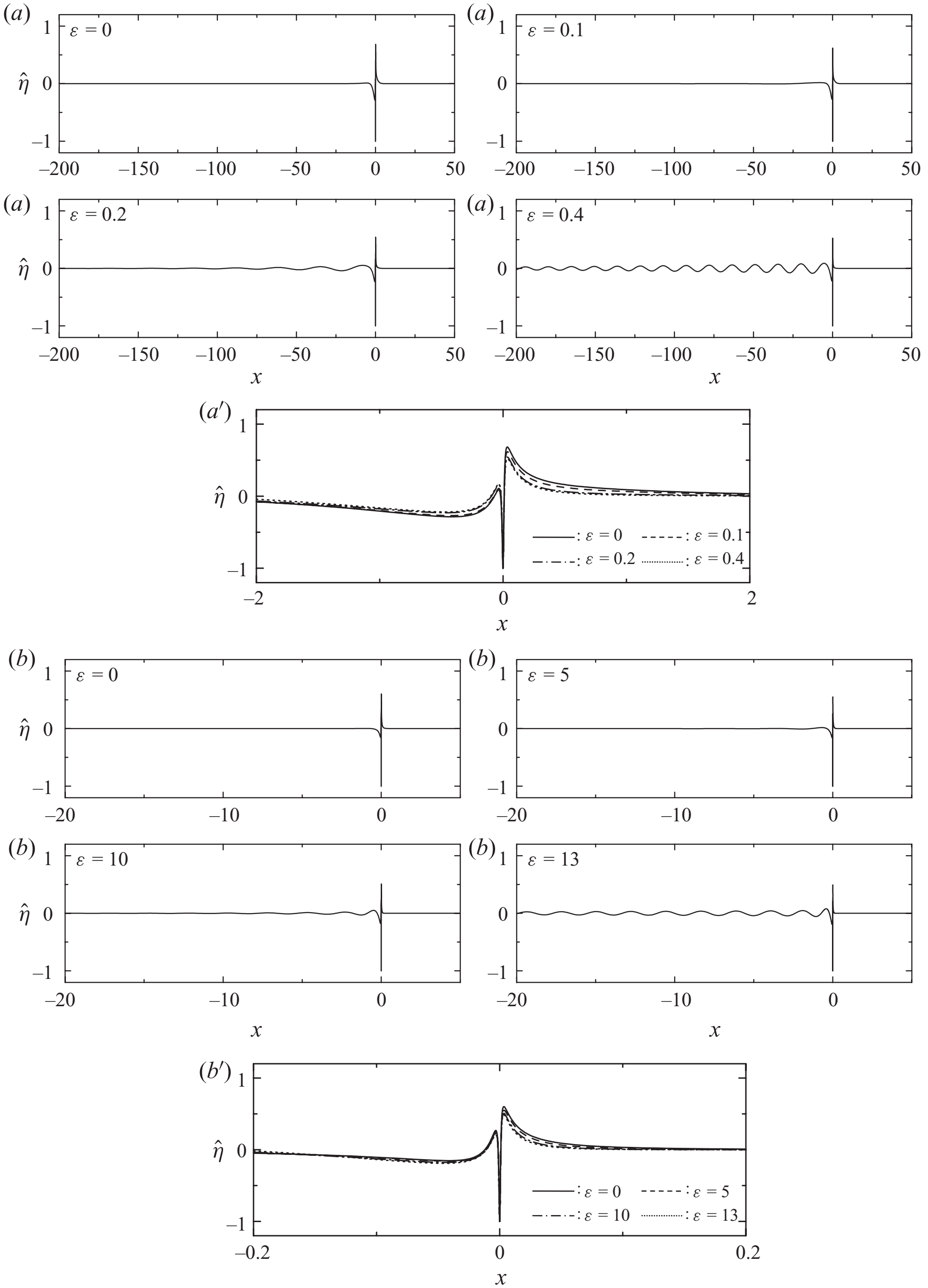

FIGURE 19. Surface profile $\hat{\eta}$ of a growing disturbance mode whose eigenvalue is on the second real branch: (*a*) $h = 0.831$ ($\varepsilon = 0$, 0.1, 0.2, 0.4); (*a*′) enlarged view of (*a*) in the core region ($-2 < x < 2$); (*b*) $h = 0.833$ ($\varepsilon = 0$, 5, 10, 13); (*b*′) enlarged view of (*b*) in the core region ($-0.2 < x < 0.2$). All profiles are numerical results normalized by (5.1), and the result for $\varepsilon = 0$ is obtained by the numerical method in Kataoka (2006*a*).

from the linear dispersion relationship (5.2) are (k_r, k_i) =(0.058, 0.11), (0.021, 0.24) and (0.006, 0.43) for $\varepsilon = 0.1$, 0.2 and 0.4, respectively, when $h = 0.831$, and (0.44, 1.8), (0.20, 2.5) and (0.03, 2.8) for $\varepsilon = 5$, 10 and 13, respectively, when $h = 0.833$. These results are consistent with those observed in surface profiles in figures 19(*a*, *b*).

6. Concluding remarks

We have numerically examined the linear transverse stability of finite-amplitude surface solitary waves on the basis of the three-dimensional Euler set of equations. Numerical results support the previous theoretical result by Kataoka & Tsutahara (2004*a*) that surface solitary waves are longitudinally stable but transversely unstable for a wave amplitude greater than 0.7133 and less than 0.7807. Eigenvalues and eigenfunctions of growing transverse disturbance modes agree well with those obtained by the theoretical asymptotic analysis for disturbances of small transverse wavenumbers. In the special cases where the energy or the wave speed of the solitary wave is near its extremum, the ordinary asymptotic solution obtained by Kataoka & Tsutahara (2004*a*) and Kataoka (2008) does not give a good approximation, and we present new asymptotic solutions valid for these cases in Appendices A and B, which show good agreement with the corresponding numerical results.

As the transverse wavenumber increases, the growth rate of the disturbance exhibits the following features. For the longitudinally stable but transversely unstable solitary waves, the growth rate, which is an increasing function for small wavenumbers, reaches a peak and finally falls to zero at some finite wavenumber. Thus, there is a high-wavenumber cutoff to the transverse instability. For the longitudinally unstable solitary waves, the dependence of the growth rate on the transverse wavenumber exhibits various complicated patterns. We have grouped them into three basic classes (Classes N, C and R) in terms of the signs of the two parameters $\mathrm{d}E/\mathrm{d}v$ and Q of the solitary wave, and further into six (N, C_0, C_1, R_0, R_1 and R_2) by distinguishing three more classes (C_1, R_1 and R_2) which occur in a limited range of wave amplitudes. Typical profiles of the growth rate versus transverse wavenumber are illustrated in figure 15.

Surface profiles of growing disturbance modes are well described by the asymptotic solution if the transverse wavenumber is small. As the transverse wavenumber increases, the surface profiles of growing disturbance modes show little change in the core region as functions of the transverse wavenumber. They are almost the same as long as the corresponding eigenvalues belong to the same branch (e.g. the first or the second real branch). Their horizontal length scale, however, diminishes considerably as the wave amplitude increases. In the region behind the core of the solitary wave, radiated waves propagate, and their motions are discussed using the linear dispersion relationship.

To the best of the author's knowledge, this is the first study conducted to clarify the transverse stability of finite-amplitude surface solitary waves numerically. The motivation comes from the discovery of longitudinally stable but transversely unstable surface solitary waves by the theoretical asymptotic analysis of Kataoka & Tsutahara (2004*a*). In fact, such longitudinally stable but transversely unstable solitary waves have also been found for the other types of solitary wave solutions. For instance, they were found for interfacial solitary wave solutions in a two-layer-fluid system (Kataoka 2008) and those in the framework of the generalized Kadomtsev–Petviashvili equation with negative dispersion (Kataoka & Tsutahara 2004*b*). It is therefore interesting to examine whether the classification of transverse instability for surface solitary waves presented in this study is also applicable to these types of solitary wave solutions. This problem on the generality of the classification is left as the subject of future work.

Appendix A. Asymptotic analysis for small ε when $|\mathrm{d}E/\mathrm{d}v| \ll 1$

We seek an asymptotic solution of (2.8)–(2.12) for small ε when $|\mathrm{d}E/\mathrm{d}v| = O(\varepsilon^{2/3})$, i.e.

$$\frac{\mathrm{d}E}{\mathrm{d}v} = \varepsilon^{2/3}\varDelta, \tag{A 1}$$

where $\varDelta$ is a given constant of the order of unity (the case where $|\mathrm{d}E/\mathrm{d}v|$ is of a different order of small magnitude from $O(\varepsilon^{2/3})$ is discussed in the last paragraph of this Appendix). At the leading order in ε, the term of $O(\varepsilon^2)$ on the right-hand side of (2.8) can be ignored, and the eigenvalue problem (2.8)–(2.12) has the following leading-order solution with $\lambda = 0$:

$$\hat{\phi} = \hat{\phi}_{C0} \equiv \frac{\partial \varPhi_s}{\partial x}, \quad \hat{\eta} = \hat{\eta}_{C0} \equiv \frac{\mathrm{d}\eta_s}{\mathrm{d}x}, \quad \lambda = 0. \tag{A 2}$$

The solution (A 2) is subjected to a slow time development if the neglected term of $O(\varepsilon^2)$ in (2.8) is recovered. We investigate the asymptotic behaviour for small ε under the assumption that its slow time development is described with a time scale of $O(\varepsilon^{-2/3})$, i.e.

$$\lambda = \varepsilon^{2/3}\lambda_1, \tag{A 3}$$

where λ_1 is an unknown constant of the order of unity. For the sake of conciseness, we use

$$\alpha = \varepsilon^{2/3} \tag{A 4}$$

in the analysis.

A.1. *Core solution*

We look for a solution of (2.8)–(2.11) with a moderate variation in x and z ($\partial\hat{\phi}/\partial x = O(\hat{\phi})$, $\partial\hat{\phi}/\partial z = O(\hat{\phi})$, and $\mathrm{d}\hat{\eta}/\mathrm{d}x = O(\hat{\eta})$), in the following power series of $\alpha (= \varepsilon^{2/3})$:

$$\hat{\phi}_C = \hat{\phi}_{C0} + \alpha\hat{\phi}_{C1} + \alpha^2\hat{\phi}_{C2} + \cdots, \quad \hat{\eta}_C = \hat{\eta}_{C0} + \alpha\hat{\eta}_{C1} + \alpha^2\hat{\eta}_{C2} + \cdots, \tag{A 5a,b}$$

where the subscript C is attached to indicate the type of solution (core solution).

Substituting (A 3) and (A 5) into (2.8)–(2.11) and arranging the same-order terms in α, we obtain a series of sets of equations for $(\hat{\phi}_{Cn}, \hat{\eta}_{Cn})$ $(n = 1, 2, \ldots)$:

$$\frac{\partial^2\hat{\phi}_{Cn}}{\partial x^2} + \frac{\partial^2\hat{\phi}_{Cn}}{\partial z^2} = F_n \equiv \begin{cases} 0 & (n = 1 \,\mathrm{and}\, 2), \\ \hat{\phi}_{Cn-3} & (n \geqslant 3), \end{cases} \tag{A 6}$$

$$L_K[\hat{\phi}_{Cn}, \hat{\eta}_{Cn}] = G_n \equiv -\lambda_1\hat{\eta}_{Cn-1} \quad \text{at} \quad z = \eta_s, \tag{A 7}$$

$$L_D[\hat{\phi}_{Cn}, \hat{\eta}_{Cn}] = H_n \equiv -\lambda_1\hat{\phi}_{Cn-1} \quad \text{at} \quad z = \eta_s, \tag{A 8}$$

$$\frac{\partial\hat{\phi}_{Cn}}{\partial z} = 0 \quad \text{at} \quad z = -1, \tag{A 9}$$

where L_K and L_D are defined by (2.13). For this set of inhomogeneous equations (A 6)–(A 9) to have a solution that does not diverge exponentially as $x \rightarrow \pm\infty$, its inhomogeneous terms F_n, G_n and H_n on the right-hand sides of (A 6)–(A 8) must satisfy the solvability condition:

$$\sum_{m=1}^{n}\alpha^m\left\{\int_{-\infty}^{\infty}\mathrm{d}x\int_{-1}^{\eta_s}\frac{\partial\Phi_s}{\partial x}F_m\mathrm{d}z+\int_{-\infty}^{\infty}\left[\frac{\partial\Phi_s}{\partial x}G_m-\frac{\mathrm{d}\eta_s}{\mathrm{d}x}H_m\right]_{z=\eta_s}\mathrm{d}x\right\}=O(\alpha^{n+1}), \tag{A 10}$$

where the quantities in the square brackets with subscript $z=\eta_s$ are evaluated at $z=\eta_s$.

For $n=1$, the solvability condition (A 10) is identically satisfied, and a solution for $n=1$ is explicitly given by

$$\hat{\phi}_{C1}=-\lambda_1\frac{\partial\Phi_s}{\partial v},\quad \hat{\eta}_{C1}=-\lambda_1\frac{\partial\eta_s}{\partial v}, \tag{A 11a,b}$$

where $\partial\Phi_s/\partial v$ and $\partial\eta_s/\partial v$ represent the derivatives of Φ_s and η_s with respect to v for fixed x and z. For $n=2$, (A 10) is identically satisfied due to (A 1), and for $n=3$ it becomes

$$\frac{\lambda_1^2\Delta}{v}+[\hat{\phi}_{C1}\hat{u}_{C2}]_{x\to\infty}-[\hat{\phi}_{C1}\hat{u}_{C2}]_{x\to-\infty}+E=O(\alpha), \tag{A 12}$$

where E is defined by (2.15) and

$$\hat{u}_{C2}=\frac{\partial\hat{\phi}_{C2}}{\partial x}-v\hat{\eta}_{C2}. \tag{A 13}$$

In (A 12), the quantities in the square brackets with subscript $x\to-\infty$ or ∞ are evaluated as $x\to-\infty$ or ∞, and use has been made of the formula (3.16) of Kataoka (2008). Here $[\hat{\phi}_{C1}]_{x\to\pm\infty}$ and $[\hat{u}_{C2}]_{x\to\pm\infty}$ appearing on the left-hand side of (A 12) satisfy the relations

$$[\hat{\phi}_{C1}]_{x\to-\infty}=[\hat{\phi}_{C1}]_{x\to\infty}-\lambda_1\frac{\mathrm{d}\Omega}{\mathrm{d}v},\quad [\hat{u}_{C2}]_{x\to-\infty}=[\hat{u}_{C2}]_{x\to\infty}-\lambda_1^2\frac{\mathrm{d}M}{\mathrm{d}v}, \tag{A 14a,b}$$

where Ω and M are defined by (2.18). We can obtain (A 14b) by integrating (A 6) for $n=2$ with respect to x and z and using (A 7) for $n=2$.

A.2. *Far-field solution*

Introducing a shrunken coordinate with respect to x,

$$X=\alpha x, \tag{A 15}$$

we seek a solution of (2.8)–(2.11) with a moderate variation in X and z ($\partial\hat{\phi}/\partial X=O(\hat{\phi})$, $\partial\hat{\phi}/\partial z=O(\hat{\phi})$, and $\mathrm{d}\hat{\eta}/\mathrm{d}X=O(\hat{\eta})$), in the following power series of α:

$$\hat{\phi}_F=\alpha\hat{\phi}_{F1}(X,z)+\alpha^2\hat{\phi}_{F2}(X,z)+\cdots,\quad \hat{\eta}_F=\alpha^2\hat{\eta}_{F2}(X)+\alpha^3\hat{\eta}_{F3}(X)+\cdots, \tag{A 16a,b}$$

where the subscript F is attached to show the type of solution (far-field solution).

Substituting (A 15) and (A 16) into (2.8)–(2.11), and arranging the same-order terms in α, we obtain a series of sets of equations for $\hat{\phi}_{Fn}$ ($n=1,2,\ldots$):

$$\frac{\partial^2\hat{\phi}_{Fn}}{\partial z^2}=I_n\equiv-\frac{\partial^2\hat{\phi}_{Fn-2}}{\partial X^2}+\hat{\phi}_{Fn-3}, \tag{A 17}$$

$$\frac{\partial\hat{\phi}_{Fn}}{\partial z}=J_n\equiv\left(\lambda_1-v\frac{\mathrm{d}}{\mathrm{d}X}\right)\hat{\eta}_{Fn-1}\quad\text{at}\quad z=0, \tag{A 18}$$

$$\frac{\partial\hat{\phi}_{Fn}}{\partial z}=0\quad\text{at}\quad z=-1, \tag{A 19}$$

where $\hat{\eta}_{Fn}$ $(n=2,3,\ldots)$ is expressed in terms of the lower-order solution $\hat{\phi}_{Fn-1}$ as

$$\hat{\eta}_{Fn} = \left[\left(v\frac{\partial}{\partial X} - \lambda_1\right)\hat{\phi}_{Fn-1}\right]_{z=0}, \tag{A 20}$$

and the quantities in the square brackets with subscript $z=0$ are evaluated at $z=0$. Note that $\hat{\phi}_{Fm}(m\leqslant 0)=0$ and $\hat{\eta}_{Fm}(m\leqslant 1)=0$ on the right-hand sides of (A 17) and (A 18). For $n=1$ and 2, the set of equations (A 17)–(A 19) for $\hat{\phi}_{Fn}$ is homogeneous and has a solution independent of z, i.e. $\hat{\phi}_{Fn}=\hat{\phi}_{Fn}(X)$ ($n=1$ and 2). For $n=3$ it is inhomogeneous, and in order to have a solution, its inhomogeneous terms I_3 and J_3 must satisfy the solvability condition $\int_{-1}^{0} I_3 \mathrm{d}z = J_3$. This condition determines the dependence of $\hat{\phi}_{F1}$ on X as

$$\hat{\phi}_{F1} = c_{1\pm}\exp\left(\frac{\lambda_1 X}{v-1}\right) + \bar{c}_{1\pm}\exp\left(\frac{\lambda_1 X}{v+1}\right), \tag{A 21}$$

where c_{1+} and $\bar{c}_{1+}$ are undetermined constants for $X>0$, and c_{1-} and $\bar{c}_{1-}$ are those for $X<0$. Note that v is larger than unity in (A 21) (see the statement before (2.6)).

A.3. *Matching*

The far-field solution $(\hat{\phi}_F, \hat{\eta}_F)$ in the core region $(|X|\ll 1)$ is expanded in power series of X (or αx) as $\hat{f}_F=(\hat{f}_F)_0+\alpha x(\partial\hat{f}_F/\partial X)_0+\alpha^2x^2(\partial^2\hat{f}_F/\partial X^2)_0/2+\cdots$, where $\hat{f}$ represents $(\hat{\phi},\hat{\eta})$ and the quantities in the parentheses with subscript 0 or $(\ )_0$ are evaluated at $X=0$. We then collect the same-order terms of α and obtain a reordered form (say, $(\hat{\phi}^*_{Fn},\hat{\eta}^*_{Fn})$) of $(\hat{\phi}_{Fn},\hat{\eta}_{Fn})$. Matching is carried out by comparing forms of the two solutions $([\hat{\phi}_{Cn}]_{x\to\pm\infty}, [\hat{\eta}_{Cn}]_{x\to\pm\infty})$ and $(\hat{\phi}^*_{Fn},\hat{\eta}^*_{Fn})$ at each n from $n=1$.

For $n=1$, since $\hat{\phi}^*_{F1}=(\hat{\phi}_{F1})_0$, matching is accomplished if

$$[\hat{\phi}_{C1}]_{x\to\pm\infty} = c_{1\pm}+\bar{c}_{1\pm}, \tag{A 22}$$

where (A 21) is used. All positive or all negative signs should be chosen in the double signs in (A 22) (and also in (A 23) below). For $n=2$, since $\hat{\phi}^*_{F2}=(\hat{\phi}_{F2})_0+x(\partial\hat{\phi}_{F1}/\partial X)_0$, there are two different kinds of terms, i.e. those independent of x and those proportional to x. The relations among those proportional to x contribute to determination of $c_{1\pm}$ and $\bar{c}_{1\pm}$. It is convenient to represent them in terms of $\hat{u}_{C2}$ defined by (A 13), i.e.

$$[\hat{u}_{C2}]_{x\to\pm\infty} = \lambda_1(\bar{c}_{1\pm}-c_{1\pm}), \tag{A 23}$$

where (A 20) and (A 21) are used. From the boundary condition (2.12) with (A 21),

$$c_{1+}=\bar{c}_{1+}=0 \quad \text{for} \quad \mathrm{Re}\,[\lambda_1]>0, \tag{A 24a}$$

$$c_{1-}=\bar{c}_{1-}=0 \quad \text{for} \quad \mathrm{Re}\,[\lambda_1]<0. \tag{A 24b}$$

The eight undetermined constants $[\hat{\phi}_{C1}]_{x\to\pm\infty}$, $[\hat{u}_{C2}]_{x\to\pm\infty}$, $c_{1\pm}$ and $\bar{c}_{1\pm}$ are determined by the eight equations (A 14), (A 22), (A 23) and (A 24*a*) or (A 24*b*). Substituting the result into (A 12), we obtain a cubic equation for λ_1, and the solution is

$$\lambda_1 = \begin{cases} \pm\dfrac{\Delta}{3vA}(1+2\cos\theta),\ \pm\dfrac{\Delta}{3vA}\left(1+2\cos\left(\theta-\dfrac{2}{3}\pi\right)\right) \\ \hfill \text{for} \quad \Delta < -3v\left(\dfrac{A^2E}{4}\right)^{1/3}, & \text{(A 25}a\text{)} \\ \pm\left[\dfrac{\Delta}{3vA}-\dfrac{1}{2}\left(B+\dfrac{\Delta^2}{9v^2A^2B}\right)\right] \pm \dfrac{\sqrt{3}\,\mathrm{i}}{2}\left(B-\dfrac{\Delta^2}{9v^2A^2B}\right) \\ \hfill \text{for} \quad \Delta > -3v\left(\dfrac{A^2E}{4}\right)^{1/3}, & \text{(A 25}b\text{)} \end{cases}$$

where any signs can be chosen in the double signs, and

$$A = -\frac{\mathrm{d}\Omega}{\mathrm{d}v}\frac{\mathrm{d}M}{\mathrm{d}v} > 0, \quad \theta = \frac{1}{3}\arctan\left(\frac{\sqrt{-1-4\Delta^3/(27v^3A^2E)}}{-1-2\Delta^3/(27v^3A^2E)}\right) \quad \left(0<\theta<\frac{\pi}{3}\right), \tag{A 26a,b}$$

$$B = \left(\frac{E}{2A}\right)^{1/3}\left(1+\frac{2\Delta^3}{27v^3A^2E}+\sqrt{1+\frac{4\Delta^3}{27v^3A^2E}}\right)^{1/3}. \tag{A 26c}$$

Here $A>0$ is used because this inequality holds at the first three extrema in E (at $h=0.7807$, 0.83028 and 0.83305). The solution (A 25b) indicates that the eigenvalues with a positive real part are complex conjugate when $\Delta>0$ (or $\mathrm{d}E/\mathrm{d}v>0$ for which h is just below the amplitude of $\mathrm{d}E/\mathrm{d}v=0$; see figure 1), whereas there are the two following patterns depending on ε when $\Delta<0$ (or $\mathrm{d}E/\mathrm{d}v<0$ for which h is just above the amplitude of $\mathrm{d}E/\mathrm{d}v=0$): (i) two positive real eigenvalues appear for $0<\varepsilon<\varepsilon_{cr}$ (see (A 25a)); (ii) complex-conjugate eigenvalues with a positive real part appear for $\varepsilon>\varepsilon_{cr}$ (see (A 25b)), where $\varepsilon_{cr}=(2/A\sqrt{E})(|\mathrm{d}E/\mathrm{d}v|/3v)^{3/2}$.

Up to now, we have considered the case of $|\mathrm{d}E/\mathrm{d}v|=O(\alpha)(=O(\varepsilon^{2/3}))$. The solution (A 25) is, however, valid for $|\mathrm{d}E/\mathrm{d}v|\ll\alpha$ and $\alpha\ll|\mathrm{d}E/\mathrm{d}v|\ll 1$. For $|\mathrm{d}E/\mathrm{d}v|\ll\alpha$ (or $|\Delta|\ll 1$), λ_1 at the leading order is simply given by (A 25b) with $\Delta=0$. For $\alpha\ll|\mathrm{d}E/\mathrm{d}v|\ll 1$ (or $|\Delta|\gg 1$), (A 25) with $|\Delta|\gg 1$ gives $\lambda_1=\pm\Delta/vA+\cdots$ and $\pm(\sqrt{-vE/\Delta}+v^2EA/2\Delta^2+\cdots)$ for $\Delta<0$, and $\lambda_1=\pm(\mathrm{i}\sqrt{vE/\Delta}\pm v^2EA/2\Delta^2+\cdots)$ for $\Delta>0$. These results are valid for $\alpha\ll|\mathrm{d}E/\mathrm{d}v|\ll 1$ because the same results are derived from substitution of (A 1) into the solution λ valid for $\mathrm{d}E/\mathrm{d}v=O(1)$ (given by (3.54) of Kataoka 2006a, and (3.18) and (3.22) with $\rho=0$ of Kataoka 2008).

Appendix B. Asymptotic analysis for small ε when $|\mathrm{d}v/\mathrm{d}h|\ll 1$

We seek an asymptotic solution of (2.8)–(2.12) for small ε when $|\mathrm{d}v/\mathrm{d}h|=O(\varepsilon^2)$, i.e.

$$\frac{\mathrm{d}v}{\mathrm{d}h}=\varepsilon^2 V, \tag{B 1}$$

where V is a given constant of the order of unity (the case where $|\mathrm{d}v/\mathrm{d}h|$ is of a different order of small magnitude from $O(\varepsilon^2)$ is discussed in the last paragraph of this Appendix). At the leading order in ε, equations (2.8)–(2.11) have the following leading-order solution with $\lambda=0$:

$$\hat{\phi}=\hat{\phi}_{C0}\equiv\frac{\partial\Phi_s}{\partial x}+\beta\frac{\partial\Phi_s}{\partial h}, \quad \hat{\eta}=\hat{\eta}_{C0}\equiv\frac{\mathrm{d}\eta_s}{\mathrm{d}x}+\beta\frac{\partial\eta_s}{\partial h}, \quad \lambda=0, \tag{B 2}$$

where β is an undetermined constant, and $\partial\Phi_s/\partial h$ and $\partial\eta_s/\partial h$ represent the derivatives of Φ_s and η_s with respect to h for fixed x and z. The λ will have non-zero small value at the higher orders, and it is assumed to be $O(\varepsilon^2)$, i.e.

$$\lambda = \varepsilon^2 \lambda_2, \tag{B 3}$$

where λ_2 is an unknown constant of the order of unity.

B.1. *Core solution*

We look for a solution of (2.8)–(2.11) with a moderate variation in x and z ($\partial\hat{\phi}/\partial x = O(\hat{\phi})$, $\partial\hat{\phi}/\partial z = O(\hat{\phi})$ and $\mathrm{d}\hat{\eta}/\mathrm{d}x = O(\hat{\eta})$), in the following power series of ε^2:

$$\hat{\phi}_C = \hat{\phi}_{C0} + \varepsilon^2 \hat{\phi}_{C2} + \varepsilon^4 \hat{\phi}_{C4} + \cdots, \qquad \hat{\eta}_C = \hat{\eta}_{C0} + \varepsilon^2 \hat{\eta}_{C2} + \varepsilon^4 \hat{\eta}_{C4} + \cdots, \tag{B 4a,b}$$

where the leading-order solution $(\hat{\phi}_{C0}, \hat{\eta}_{C0})$ is given by (B 2).

Substituting (B 3) and (B 4) into (2.8)–(2.11) and arranging the same-order terms in ε^2, we obtain a series of sets of equations for $(\hat{\phi}_{Cn}, \hat{\eta}_{Cn})$ $(n = 2, 4, \ldots)$. For $n = 2$, it becomes

$$\frac{\partial^2 \hat{\phi}_{C2}}{\partial x^2} + \frac{\partial^2 \hat{\phi}_{C2}}{\partial z^2} = F_2 \equiv \frac{\partial \Phi_s}{\partial x} + \beta \frac{\partial \Phi_s}{\partial h}, \tag{B 5}$$

$$L_K[\hat{\phi}_{C2}, \hat{\eta}_{C2}] = G_2 \equiv -\lambda_2 \left(\frac{\mathrm{d}\eta_s}{\mathrm{d}x} + \beta \frac{\partial \eta_s}{\partial h} \right) - \beta V \frac{\mathrm{d}\eta_s}{\mathrm{d}x} \quad \text{at} \quad z = \eta_s, \tag{B 6}$$

$$L_D[\hat{\phi}_{C2}, \hat{\eta}_{C2}] = H_2 \equiv -\lambda_2 \left(\frac{\partial \Phi_s}{\partial x} + \beta \frac{\partial \Phi_s}{\partial h} \right) - \beta V \frac{\partial \Phi_s}{\partial x} \quad \text{at} \quad z = \eta_s, \tag{B 7}$$

$$\frac{\partial \hat{\phi}_{C2}}{\partial z} = 0 \quad \text{at} \quad z = -1, \tag{B 8}$$

where L_K and L_D are defined by (2.13). For this set of inhomogeneous equations (B 5)–(B 8) to have a solution that does not diverge exponentially as $x \to \pm\infty$, its inhomogeneous terms F_2, G_2 and H_2 on the right-hand sides of (B 5)–(B 7) must satisfy the solvability conditions:

$$\int_{-\infty}^{\infty} \mathrm{d}x \int_{-1}^{\eta_s} \frac{\partial \Phi_s}{\partial x} F_2 \mathrm{d}z + \int_{-\infty}^{\infty} \left[\frac{\partial \Phi_s}{\partial x} G_2 - \frac{\mathrm{d}\eta_s}{\mathrm{d}x} H_2 \right]_{z=\eta_s} \mathrm{d}x = 0, \tag{B 9a}$$

$$\int_{-\infty}^{\infty} \mathrm{d}x \int_{-1}^{\eta_s} \frac{\partial \Phi_s}{\partial h} F_2 \mathrm{d}z + \int_{-\infty}^{\infty} \left[\frac{\partial \Phi_s}{\partial h} G_2 - \frac{\partial \eta_s}{\partial h} H_2 \right]_{z=\eta_s} \mathrm{d}x$$
$$= \left[\frac{\partial \Phi_s}{\partial h} \left(\frac{\partial \hat{\phi}_{C2}}{\partial x} - v \hat{\eta}_{C2} \right) \right]_{x \to \infty} - \left[\frac{\partial \Phi_s}{\partial h} \left(\frac{\partial \hat{\phi}_{C2}}{\partial x} - v \hat{\eta}_{C2} \right) \right]_{x \to -\infty}, \tag{B 9b}$$

where the quantities in the square brackets with subscript $z = \eta_s$ or $x \to -\infty$ (or ∞) are evaluated at $z = \eta_s$ or $x \to -\infty$ (or ∞), respectively. Noting that $\Phi_s(x, z) - \Phi_s(0, z)$ is odd in x (see the statement after (2.6)) and $\Phi_s(0, z) = (\Phi_s(-\infty, z) + \Phi_s(\infty, z))/2$, we find that (B 9) become

$$-\frac{\lambda_2\beta}{v}\frac{\mathrm{d}E}{\mathrm{d}h}+E=-\frac{vM}{2}\left([\hat{\phi}_{C0}]_{x\to-\infty}+[\hat{\phi}_{C0}]_{x\to\infty}\right), \tag{B 10a}$$

$$\begin{aligned}\frac{\beta^2 V}{v}\frac{\mathrm{d}E}{\mathrm{d}h}+E+\beta^2\int_{-\infty}^{\infty}\mathrm{d}x\int_{-1}^{\eta_s}\left(\frac{\partial\Phi_s}{\partial h}-\left[\frac{\partial\Phi_s}{\partial h}\right]_{x\to-\infty}\right)\left(\frac{\partial\Phi_s}{\partial h}-\left[\frac{\partial\Phi_s}{\partial h}\right]_{x\to\infty}\right)\mathrm{d}z\\ =-\left[\hat{\phi}_{C0}\left(\hat{u}_{C2}+\frac{M}{2}\hat{\phi}_{C0}+vM\right)\right]_{x\to-\infty}+\left[\hat{\phi}_{C0}\left(\hat{u}_{C2}-\frac{M}{2}\hat{\phi}_{C0}-vM\right)\right]_{x\to\infty},\end{aligned} \tag{B 10b}$$

where E and M are defined by (2.15) and (2.18), and

$$\hat{u}_{C2}=\frac{\partial\hat{\phi}_{C2}}{\partial x}-v\hat{\eta}_{C2}-x\hat{\phi}_{C0}. \tag{B 11}$$

Here $[\hat{\phi}_{C0}]_{x\to\pm\infty}$ and $[\hat{u}_{C2}]_{x\to\pm\infty}$ appearing on the right-hand sides of (B 10) satisfy the relations

$$[\hat{\phi}_{C0}]_{x\to-\infty}=[\hat{\phi}_{C0}]_{x\to\infty}+\beta\frac{\mathrm{d}\Omega}{\mathrm{d}h}, \tag{B 12a}$$

$$\left[\hat{u}_{C2}+\frac{M}{2}\hat{\phi}_{C0}\right]_{x\to-\infty}=\left[\hat{u}_{C2}-\frac{M}{2}\hat{\phi}_{C0}\right]_{x\to\infty}-vM+\lambda_2\beta\frac{\mathrm{d}M}{\mathrm{d}h}, \tag{B 12b}$$

where Ω is defined by (2.18).

B.2. *Far-field solution*

Introducing two shrunken coordinates with respect to x,

$$X=\varepsilon x,\quad X_2=\varepsilon^2 x, \tag{B 13a,b}$$

we look for a solution of (2.8)–(2.11) with a moderate variation in X, X_2 and z in the following power series of ε:

$$\hat{\phi}_F=\hat{\phi}_{F0}(X,X_2,z)+\varepsilon\hat{\phi}_{F1}(X,X_2,z)+\cdots,\quad \hat{\eta}_F=\varepsilon\hat{\eta}_{F1}(X,X_2)+\varepsilon^2\hat{\eta}_{F2}(X,X_2)+\cdots. \tag{B 14a,b}$$

Substituting (B 13) and (B 14) into (2.8)–(2.11), and arranging the same-order terms in ε, we obtain a series of sets of equations for $\hat{\phi}_{Fn}$ ($n=0,1,2,\dots$):

$$\frac{\partial^2\hat{\phi}_{Fn}}{\partial z^2}=I_n\equiv\hat{\phi}_{Fn-2}-\frac{\partial^2\hat{\phi}_{Fn-2}}{\partial X^2}-2\frac{\partial^2\hat{\phi}_{Fn-3}}{\partial X\partial X_2}-\frac{\partial^2\hat{\phi}_{Fn-4}}{\partial X_2^2}, \tag{B 15}$$

$$\frac{\partial\hat{\phi}_{Fn}}{\partial z}=J_n\equiv-v\frac{\partial\hat{\eta}_{Fn-1}}{\partial X}+\left(\lambda_2-v\frac{\partial}{\partial X_2}\right)\hat{\eta}_{Fn-2}\quad\text{at}\quad z=0, \tag{B 16}$$

$$\frac{\partial\hat{\phi}_{Fn}}{\partial z}=0\quad\text{at}\quad z=-1, \tag{B 17}$$

where $\hat{\eta}_{Fn}$ ($n=1,2,\dots$) is expressed in terms of the lower-order solutions $\hat{\phi}_{Fn-1}$ and $\hat{\phi}_{Fn-2}$ as

$$\hat{\eta}_{Fn}=\left[v\frac{\partial\hat{\phi}_{Fn-1}}{\partial X}+\left(v\frac{\partial}{\partial X_2}-\lambda_2\right)\hat{\phi}_{Fn-2}\right]_{z=0}, \tag{B 18}$$

and the quantities in the square brackets with subscript $z=0$ are evaluated at $z=0$. Note that $\hat{\phi}_{Fm}(m\leqslant-1)=0$ and $\hat{\eta}_{Fm}(m\leqslant0)=0$ on the right-hand sides of (B 15), (B 16), and (B 18). For $n=0$ and 1, the set of equations (B 15)–(B 17) is homogeneous and has a solution independent of z, i.e. $\hat{\phi}_{Fn}=\hat{\phi}_{Fn}(X,X_2)$ ($n=0$ and 1). For $n\geqslant 2$, it is inhomogeneous, and in order to have a solution, its inhomogeneous terms I_n and J_n must satisfy the solvability condition $\int_{-1}^{0} I_n\mathrm{d}z=J_n$. This condition for $n=2$ and that for $n=3$ determine the dependence of $\hat{\phi}_{F0}$ on X and X_2 as

$$\hat{\phi}_{F0}=\left[c_{0\pm}\exp\left(\frac{\mathrm{i}X}{\sqrt{v^2-1}}\right)+\bar{c}_{0\pm}\exp\left(\frac{-\mathrm{i}X}{\sqrt{v^2-1}}\right)\right]\exp\left(\frac{v\lambda_2}{v^2-1}X_2\right), \tag{B 19}$$

and the above conditions for $n=3$ and 4 determine the dependence of $\hat{\phi}_{F1}$ on X and X_2 as

$$\begin{aligned}\hat{\phi}_{F1}=\Bigg\{&\left[c_{1\pm}-\frac{\mathrm{i}c_{0\pm}}{2(v^2-1)^{3/2}}\left(\lambda_2^2+\frac{v^4}{3(v^2-1)}\right)X_2\right]\exp\left(\frac{\mathrm{i}X}{\sqrt{v^2-1}}\right)\\&+\left[\bar{c}_{1\pm}+\frac{\mathrm{i}\bar{c}_{0\pm}}{2(v^2-1)^{3/2}}\left(\lambda_2^2+\frac{v^4}{3(v^2-1)}\right)X_2\right]\exp\left(\frac{-\mathrm{i}X}{\sqrt{v^2-1}}\right)\Bigg\}\exp\left(\frac{v\lambda_2}{v^2-1}X_2\right),\end{aligned} \tag{B 20}$$

where c_{0+}, $\bar{c}_{0+}$, c_{1+} and $\bar{c}_{1+}$ are undetermined constants for $X, X_2>0$ and c_{0-}, $\bar{c}_{0-}$, c_{1-} and $\bar{c}_{1-}$ are those for $X, X_2<0$. In deriving (B 20), the solution $\hat{\phi}_{F2}$ of (B 15)–(B 17) for $n=2$ is used.

B.3. *Matching*

The far-field solution $(\hat{\phi}_F,\hat{\eta}_F)$ in the core region ($|X|\ll 1$, $|X_2|\ll 1$) being expanded in power series of X and X_2 (or εx and $\varepsilon^2 x$), and the same-order terms of ε being collected, we obtain a reordered form (say, $(\hat{\phi}^*_{Fn},\hat{\eta}^*_{Fn})$) of $(\hat{\phi}_{Fn},\hat{\eta}_{Fn})$. Matching is carried out by comparing forms of the two solutions ($[\hat{\phi}_{Cn}]_{x\to\pm\infty}$, $[\hat{\eta}_{Cn}]_{x\to\pm\infty}$) and $(\hat{\phi}^*_{Fn},\hat{\eta}^*_{Fn})$ at each n from $n=0$.

For $n=0$, since $\hat{\phi}^*_{F0}=(\hat{\phi}_{F0})_0$ (the quantities in the parentheses with subscript 0 are evaluated at $X=X_2=0$), matching is accomplished if

$$[\hat{\phi}_{C0}]_{x\to\pm\infty}=c_{0\pm}+\bar{c}_{0\pm}, \tag{B 21}$$

where (B 19) is used. All positive or all negative signs should be chosen in the double signs in (B 21) (and also in (B 22) and (B 23) below). For $n=1$, since $\hat{\phi}^*_{F1}=(\hat{\phi}_{F1})_0+x(\partial\hat{\phi}_{F0}/\partial X)_0$, matching conditions are obtained individually from two different kinds of terms, those independent of x and those proportional to x, as

$$0=c_{1\pm}+\bar{c}_{1\pm},\quad 0=c_{0\pm}-\bar{c}_{0\pm}. \tag{B 22a,b}$$

Here $\hat{\phi}_{C1}=0$, (B 19) and (B 20) are used. For $n=2$, since $\hat{\phi}^*_{F2}=(\hat{\phi}_{F2})_0+x(\partial\hat{\phi}_{F1}/\partial X+\partial\hat{\phi}_{F0}/\partial X_2)_0+(x^2/2)(\partial^2\hat{\phi}_{F0}/\partial X^2)_0$, there are three different kinds of terms. The relations among those proportional to x contribute to determination of the unknowns $c_{1\pm}$ and $\bar{c}_{1\pm}$. In view of (B 10b), it is convenient to represent them in terms of $\hat{u}_{C2}$ defined by (B 11) as

$$[\hat{u}_{C2}]_{x\to\pm\infty}=\mathrm{i}\sqrt{v^2-1}\left(-c_{1\pm}+\bar{c}_{1\pm}\right), \tag{B 23}$$

where (B 18)–(B 20) are used. From the boundary condition (2.12) with (B 19) and (B 20),

$$c_{0+}=c_{1+}=0\quad\text{for}\quad \mathrm{Re}\,[\lambda_2]>0, \tag{B 24a}$$

$$c_{0-}=c_{1-}=0\quad\text{for}\quad \mathrm{Re}\,[\lambda_2]<0, \tag{B 24b}$$

where $\bar{c}_{0+} = \bar{c}_{1+} = 0$ in (B 24*a*) and $\bar{c}_{0-} = \bar{c}_{1-} = 0$ in (B 24*b*) are already included in (B 22). The 12 undetermined constants $[\hat{\phi}_{C0}]_{x\to\pm\infty}$, $[\hat{u}_{C2}]_{x\to\pm\infty}$, $c_{0\pm}$, $\bar{c}_{0\pm}$, $c_{1\pm}$, and $\bar{c}_{1\pm}$ are determined by the 12 equations (B 12), (B 21)–(B 23) and (B 24*a*) or (B 24*b*). Substituting the result into (B 10), we obtain a quadratic equation for λ_2, and the solution is

$$\lambda_2 = \begin{cases} \pm\left(\sqrt{-\dfrac{vEV}{\mathrm{d}E/\mathrm{d}h} + Q^2 - R} - Q\right) & \text{for} \quad \dfrac{V}{\mathrm{d}E/\mathrm{d}h} < -\dfrac{R}{vE} (< 0), \qquad \text{(B 25}a\text{)} \\ \pm\left(\sqrt{-\dfrac{vEV}{\mathrm{d}E/\mathrm{d}h} + Q^2 - R} \pm Q\right) & \\ & \text{for} \quad -\dfrac{R}{vE} < \dfrac{V}{\mathrm{d}E/\mathrm{d}h} < \dfrac{Q^2 - R}{vE} (< 0), \qquad \text{(B 25}b\text{)} \\ \pm\left(\mathrm{i}\sqrt{\dfrac{vEV}{\mathrm{d}E/\mathrm{d}h} + R - Q^2} \pm Q\right) & \text{for} \quad \dfrac{V}{\mathrm{d}E/\mathrm{d}h} > \dfrac{Q^2 - R}{vE} (< 0), \qquad \text{(B 25}c\text{)} \end{cases}$$

where Q is defined by (2.17) and

$$R = \frac{v^2}{(\mathrm{d}E/\mathrm{d}h)^2}\left\{\frac{v^2M^2}{4}\left(\frac{\mathrm{d}\Omega}{\mathrm{d}h}\right)^2 + E\int_{-\infty}^{\infty}\mathrm{d}x\int_{-1}^{\eta_s}\left(\frac{\partial\Phi_s}{\partial h} - \left[\frac{\partial\Phi_s}{\partial h}\right]_{x\to-\infty}\right)\right. \\ \left. \times\left(\frac{\partial\Phi_s}{\partial h} - \left[\frac{\partial\Phi_s}{\partial h}\right]_{x\to\infty}\right)\mathrm{d}z\right\}. \qquad \text{(B 26)}$$

Inequalities $Q < 0$ and $Q^2 < R$ are used in (B 25) since they hold at the first three extrema in v (at $h = 0.79591$, 0.8309762 and 0.83308). Any signs can be chosen in the double signs in (B 25). The solution (B 25*c*) indicates that the eigenvalues with a positive real part are complex conjugate when $V/(\mathrm{d}E/\mathrm{d}h) > 0$ (or $\mathrm{d}E/\mathrm{d}v > 0$ for which h is just above the amplitude of $\mathrm{d}v/\mathrm{d}h = 0$; see figure 1), whereas there are the three following patterns depending on ε when $V/(\mathrm{d}E/\mathrm{d}h) < 0$ (or $\mathrm{d}E/\mathrm{d}v < 0$ for which h is just below the amplitude of $\mathrm{d}v/\mathrm{d}h = 0$): (i) only a single positive real eigenvalue exists for $\varepsilon < \varepsilon_{cr1}$ (see (B 25*a*)); (ii) two positive real eigenvalues appear for $\varepsilon_{cr1} < \varepsilon < \varepsilon_{cr2}$ (see (B 25*b*)); (iii) complex-conjugate eigenvalues with a positive real part appear for $\varepsilon > \varepsilon_{cr2}$ (see (B 25*c*)), where $\varepsilon_{cr1} = \sqrt{vE/|R\mathrm{d}E/\mathrm{d}v|}$ and $\varepsilon_{cr2} = \sqrt{vE/|(R - Q^2)\mathrm{d}E/\mathrm{d}v|}$.

Up to now, we have considered the case of $|\mathrm{d}v/\mathrm{d}h| = O(\varepsilon^2)$. The solution (B 25) is, however, valid for $|\mathrm{d}v/\mathrm{d}h| \ll \varepsilon^2$ and $\varepsilon^2 \ll |\mathrm{d}v/\mathrm{d}h| \ll 1$. For $|\mathrm{d}v/\mathrm{d}h| \ll \varepsilon^2$ (or $|V| \ll 1$), λ_2 at the leading order is simply given by (B 25*c*) with $V = 0$. For $\varepsilon^2 \ll |\mathrm{d}v/\mathrm{d}h| \ll 1$ (or $|V| \gg 1$), (B 25*a*,*c*) with $|V| \gg 1$ gives $\lambda_2 = \pm(\sqrt{-vEV/(\mathrm{d}E/\mathrm{d}h)} - Q + \cdots)$ for $V/(\mathrm{d}E/\mathrm{d}h) < 0$, and $\lambda_2 = \pm(\mathrm{i}\sqrt{vEV/(\mathrm{d}E/\mathrm{d}h)} \pm Q + \cdots)$ for $V/(\mathrm{d}E/\mathrm{d}h) > 0$. These results are valid for $\varepsilon^2 \ll |\mathrm{d}v/\mathrm{d}h| \ll 1$ because the same results are derived from substitution of (B 1) into the solution λ valid for $\mathrm{d}v/\mathrm{d}h = O(1)$ (given by (3.18) and (3.22) with $\rho = 0$ of Kataoka 2008).

REFERENCES

Alexander, J. C., Pego, R. L. & Sachs, R. L. 1997 On the transverse instability of solitary waves in the Kadomtsev–Petviashivili equation. *Phys. Lett.* A **226**, 187–192.

Allen, M. A. & Rowlands, G. 1997 On the transverse instabilities of solitary waves. *Phys. Lett.* A **235**, 145–146.

Amick, C. J. & Toland, J. F. 1981 On solitary water-waves of finite amplitude. *Arch. Ration. Mech. Anal.* **76**, 9–95.

Benjamin, T. B. 1972 The stability of solitary waves. *Proc. R. Soc. Lond.* A **328**, 153–183.

Bridges, T. J. 2001 Transverse instability of solitary-wave states of the water-wave problem. *J. Fluid Mech.* **439**, 255–278.

Byatt-Smith, J. G. & Longuet-Higgins, M. S. 1976 On the speed and profile of steep solitary waves. *Proc. R. Soc. Lond.* A **350**, 175–189.

Craig, W. & Sternberg, P. 1988 Symmetry of solitary waves. *Commun. Partial Differ. Equ.* **13**, 603–633.

Jeffrey, A. & Kakutani, T. 1970 Stability of the Burgers shock wave and the Korteweg–de Vries soliton. *Indiana Univ. Math. J.* **20**, 463–468.

Kadomtsev, B. B. & Petviashvili, V. I. 1970 On the stability of solitary waves in a weakly dispersing medium. *Sov. Phys. Dokl.* **15**, 539–541.

Kataoka, T. 2006*a* The stability of finite-amplitude interfacial solitary waves. *Fluid Dyn. Res.* **38**, 831–867.

Kataoka, T. 2006*b* On the superharmonic instability of surface gravity waves on fluid of finite depth. *J. Fluid Mech.* **547**, 175–184.

Kataoka, T. 2008 Transverse instability of interfacial solitary waves. *J. Fluid Mech.* **611**, 255–282.

Kataoka, T. & Tsutahara, M. 2004*a* Transverse instability of surface solitary waves. *J. Fluid Mech.* **512**, 211–221.

Kataoka, T. & Tsutahara, M. 2004*b* Instability of solitary wave solutions to long-wavelength transverse perturbations in the generalized Kadomtsev–Petviashvili equation with negative dispersion. *Phys. Rev.* E **70**, 016604.

Kivshar, Y. S. & Pelinovsky, D. E. 2000 Self-focusing and transverse instabilities of solitary waves. *Phys. Rep.* **331**, 117–195.

Kuznetsov, E. A., Spector, M. D. & Fal'Kovich, G. E. 1984 On the stability of nonlinear waves in integrable models. *Physica* D **10**, 379–386.

Longuet-Higgins, M. S. & Fox, M. J. H. 1996 Asymptotic theory for the almost-highest solitary wave. *J. Fluid Mech.* **317**, 1–19.

Longuet-Higgins, M. S. & Tanaka, M. 1997 On the crest instabilities of steep surface waves. *J. Fluid Mech.* **336**, 51–68.

McLean, J. W. 1982*a* Instabilities of finite-amplitude water waves. *J. Fluid Mech.* **114**, 315–330.

McLean, J. W. 1982*b* Instabilities of finite-amplitude gravity waves on water of finite depth. *J. Fluid Mech.* **114**, 331–341.

Saffman, P. G. 1985 The superharmonic instability of finite-amplitude water waves. *J. Fluid Mech.* **159**, 169–174.

Tanaka, M. 1986 The stability of solitary waves. *Phys. Fluids* **29**, 650–655.

Tanaka, M., Dold, J. W., Lewy, M. & Peregrine, D. H. 1987 Instability and breaking of a solitary wave. *J. Fluid Mech.* **185**, 235–248.

Turner, R. E. L. & Vanden-Broeck, J.-M. 1988 Broadening of interfacial solitary waves. *Phys. Fluids* **31**, 2486–2490.

Wilkinson, J. H. 1965 *The Algebraic Eigenvalue Problem.* Oxford University Press.

Zakharov, V. E. 1975 Instability and nonlinear oscillations of solitons. *JETP Lett.* **22**, 172–173.